J. Fluid Mech. (2025), *vol.* 1015, A11, doi:10.1017/jfm.2025.10321

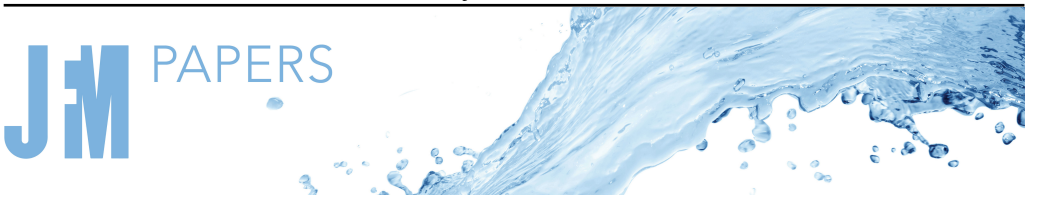

A numerical investigation of airfoil tonal noise reduction by roughness elements

Zhenyang Yuan[1], **Elías Alva**[2], **Tiago B. de Araújo**[2], **André V.G. Cavalieri**[2] **and Ardeshir Hanifi**[1]

[1]FLOW, Department of Engineering Mechanics, KTH Royal Institute of Technology, Stockholm, Sweden
[2]Divisão de Engenharia Aeronáutica, Instituto Tecnológico de Aeronáutica, São José dos Campos, Brazil
Corresponding author: Zhenyang Yuan, zhenyang@kth.se

(Received 10 October 2024; revised 21 May 2025; accepted 2 June 2025)

In a combined experimental and numerical effort, we investigate the generation and reduction of airfoil tonal noise. The means of noise control are streak generators in the form of cylindrical roughness elements. These elements are placed periodically along the span of the airfoil at the mid-chord streamwise position. Experiments are performed for a wide range of Reynolds numbers and angles of attack in a companion work (Alva *et al.*, AIAA *Aviation Forum*, 2023). In the present work, we concentrate on numerical investigations for a further investigation of selected cases. We have performed wall-resolved large-eddy simulations for a NACA 0012 airfoil at zero angle of attack and Mach 0.3. Two Reynolds numbers (0.8×10^5 and 1.0×10^5) have been investigated, showing acoustic results consistent with experiments at the same Reynolds but lower Mach numbers. Roughness elements attenuate tones in the acoustic field and, for the higher Reynolds number, suppress them. Through Fourier decomposition and spectral proper orthogonal decomposition analysis of streamwise velocity data, dominating structures have been identified. Further, the coupling between the structures generated by the surface roughness and the instability modes (Kelvin–Helmholtz) of the shear layer has been identified through stability analysis, suggesting stabilisation mechanisms by which the sound generation by the airfoil is reduced by the roughness elements.

Key words: aeroacoustics, noise control

1. Introduction

Trailing-edge noise, often referred to as airfoil self-noise, is a key factor contributing to noise pollution, particularly relevant in aviation and wind energy applications. This issue is especially pertinent for communities situated near airports or wind farms. For relatively low Reynolds numbers, the trailing-edge noise also occurs in many applications, such as drones. As drones become increasingly popular and widespread, their noise emissions are emerging as a significant contributor to noise pollution, especially in urban environments, which can be disruptive to both human and wildlife populations. Due to its considerable impact, there are focused efforts to thoroughly understand, accurately model and effectively mitigate trailing-edge noise. Such initiatives aim to develop technologies that are not only quieter, but also more eco-friendly. Trailing-edge noise is generated due to the interaction between an airfoil blade and the turbulence produced in its own boundary layer and near wake (Brooks, Pope & Marcolini 1989) and is one of the main sources of noise pollution for airfoils moving through non-turbulent flows.

Tonal noise, often induced by airfoils at low to moderate Reynolds number (Arbey & Bataille 1983), is well studied in the aeroacoustic community. Compared with broadband noise, tonal noise always shows as sharp peaks in the acoustic spectrum. Those peaks are always several decibels higher than the broadband noise and, thus, more displeasing and harmful to human ears. An improved understanding of the noise generation mechanism can lead to effective control strategies for noise elimination or abatement.

In the early research on the tonal noise produced by airfoils, Paterson *et al.* (1973) identified ladder-like structures where the spectrum contains the main tone (also denoted as the primary tone (Arcondoulis *et al.* 2010)) and secondary tones by the side of the main tone. Tam (1974) suggested that the ladder-like structure is due to a self-excited feedback loop between disturbances in the boundary layer and the airfoil wake. In subsequent work, Arbey & Bataille (1983) explained the phenomenon as the result of a feedback mechanism involving instability waves in the boundary layer and acoustic waves that are scattered at the trailing edge and travel upstream, exciting the instability waves and thus closing the loop. Linear analysis by Fosas de Pando *et al.* (2014) and Ricciardi, Wolf & Taira (2022) confirms the said mechanism.

The regime of the tonal noise on an airfoil with laminar and turbulent flows has been studied by Pröbsting *et al.* (2015). The study shows that the regimes of tonal noise generation can be separated into pressure- and suction-side-dominated regions. This provides a condition for amplified spanwise-coherent vortical structures at the pressure or suction side of the airfoil. Such structures will eventually pass by the trailing edge which induce or contribute to acoustic tonal noise radiation. Experiments with forced transition to turbulence show that at lower Reynolds number tonal noise emission is dominated by the suction side, while at higher Reynolds number the emission is dominated by the pressure side.

Various approaches have been proposed for reducing trailing-edge tonal noise, including the use of leading-edge and trailing-edge serrations (Oerlemans *et al.* 2009; Hansen, Kelso & Doolan 2010; Roger *et al.* 2013; Vathylakis, Chong & Joseph 2015; Chen *et al.* 2016). These techniques primarily involve geometric adjustments to the leading or trailing edge, aiming to influence the overall aerodynamics (Serson, Meneghini & Sherwin 2017) or altering the scattering at the trailing edge (Howe 1991). However, the potential to directly modify the instability mechanisms of laminar separation bubbles has not yet been explored to the best of our knowledge.

Another promising idea for controlling tonal noise generation is to attenuate spanwise-coherent structures, as tonal noise in airfoils is mostly related to two-dimensional

disturbances (Ricciardi *et al.* 2022). In the work of Fransson *et al.* (2005), experiments show that stable and symmetric, close-to-sinusoidal, streaks of moderate amplitudes (12 % of the free-stream velocity) can stabilise Tollmien–Schlichting (T–S) waves. The streaks are generated by means of a spanwise array of cylindrical roughness elements. In the study, the stabilising effect of the streaks on T–S waves is unambiguously confirmed by increasing the height of the roughness elements. Numerical simulations (Cossu & Brandt 2002) and linear stability analyses (Cossu & Brandt 2004; Bagheri & Hanifi 2007) also confirm the stabilising effect of streaks on T–S waves at least up to a local Reynolds number (R) of 1000, where R is given by $R = \sqrt{XRe_L}$, in which Re_L is a constant and X is the streamwise location. Furthermore, this stabilisation is due to the spanwise-averaged part of the nonlinear base flow distortion induced by the streaks and occurs for streak amplitudes lower than the critical threshold beyond which secondary inflectional instability is observed. This modulated T–S wave has an almost identical phase speed to but a lower growth rate than the corresponding two-dimensional T–S waves.

In the work of Marant & Cossu (2018), it is also shown that streaks can stabilise Kelvin–Helmholtz (K–H) instabilities. When forced with finite amplitudes, the streaks modify the characteristics of the K–H instability. The maximum temporal growth rates are reduced by optimal sinuous perturbations and are slightly increased by varicose suboptimal ones. In contrast, the onset of absolute instability is delayed by varicose suboptimal perturbations and is slightly promoted by sinuous optimal ones. Besides modifying K–H instabilities, streaks can render separation bubbles three-dimensional, as explored by Karp & Hack (2020).

Direct numerical simulation of trailing-edge noise is a relatively new research topic. Wang & Moin (2000), Singer *et al.* (2000) and Manoha, Troff & Sagaut (2000) were among the first to use incompressible large-eddy simulations (LES) to compute the near-field unsteady flow around blades or thick plates and to use the acoustic analogy of Ffowcs Williams & Hall (1970) to predict the far-field acoustic sound. More recently, other acoustic analogies, i.e. the Curle (1955) and Ffowcs Williams and Hawkings formulations, have been used for far-field acoustic prediction. With increasing computational power and more modern computational fluid dynamic codes, direct simulation of far-field acoustics becomes possible. Desquesnes, Terracol & Sagaut (2007) were the first to investigate the tonal noise phenomenon occurring in the flow past two-dimensional laminar airfoils using direct numerical simulations. And later, Sandberg, Jones & Sandham (2008), Jones & Sandberg (2010) and Sandberg (2013) conducted direct numerical simulations of transitional/turbulent flow at moderate Reynolds number past NACA 0012 airfoils at different angles of attack. They investigated mechanisms of noise generation, attempting to identify sources of airfoil noise other than trailing-edge noise.

Inspired by the results stated above, we investigate the tonal noise generation of airfoils and its control through experimental and numerical studies. The means of control is a row of spanwise periodically placed cylindrical roughness elements. These roughness elements, if not too large, generate laminar streaky structures, which are expected to cause modulation and weakening of two-dimensional structures over the wing. However, the introduction of roughness elements to the geometry, including edges with the potential of additional acoustic scattering, could potentially lead to an increase in sound radiation. Thus, one cannot be sure *a priori* if the introduction of roughness elements reduces or increases the airfoil tonal noise. In the first part of the current work, reported in the companion paper (Alva *et al.* 2023), a series of experiments with different Reynolds numbers and angles of attack have been conducted for a NACA 0012 airfoil. In these experiments, both clean airfoils and those with periodically placed roughness elements have been investigated. The critical roughness Reynolds number ($Re_{kk} = U_k k \rho_k / \mu_k$,

where k is the roughness height and subscript k represents quantities at the roughness height) based on roughness height has been controlled to be $Re_{kk} = 366$ to make sure that the boundary layer will not be tripped directly by the roughness for the case with chord-based $Re = 1\,00\,000$ in the simulation. According to the calculations from Fransson *et al.* (2005) on a flat-plate boundary layer, our Re_{kk} is far less than the critical $Re_{kk} = 420$. At low Reynolds number, i.e. $Re = 80\,000$, both geometries can generate tonal noise. Lower amplitude and different frequency of tonal noise are detected in the set-up with roughness elements. At a slightly higher Reynolds number, i.e. $Re = 1\,00\,000$, the tonal noise has been almost eliminated by the roughness elements. Similar to Pröbsting *et al.* (2015), at different angles of attack, the trailing-edge noise is dominated by either pressure-side or suction-side coherent structures, which can be inferred by studying the effects of pressure- and suction-side roughness on the sound radiation separately.

In the present work, we try to investigate the mechanism of tonal noise attenuation or elimination in the presence of streaks generated by roughness elements. A series of wall-resolved LES are performed to study the problem. The problem set-up analysed here is the same as in the experiments, namely a NACA 0012 airfoil at zero angle of incidence and chord-based Reynolds number $Re = 80\,000$ and $1\,00\,000$. This configuration is prone to a strong laminar separation bubble until the trailing edge. Note that due to the slow convergence of numerical simulations at very low Mach numbers, the simulations are performed at a higher Mach number of 0.3 compared with the experiments. The airfoils both with and without the surface roughness elements are investigated and compared. Four cases in the following context are referred to as $Re = 80$k clean, $Re = 80$k rough, $Re = 100$k clean and $Re = 100$k rough, respectively. Details of the numerical simulation tools and methodology of analysis are presented in § 2. Section 3 contains the results of the fluid dynamics and acoustic measurements. Finally, data-driven spectral proper orthogonal decomposition (SPOD) and stability analyses at selected streamwise positions are carried out in order to understand the influence of the structures generated by the roughness elements on the flow. These analyses are presented in § 4. The paper is completed with conclusions in § 5.

2. Numerical set-up

2.1. *Flow configuration*

Prior to the simulation, a series of experiments have been performed. In order to be consistent with the experimental set-up, the airfoil profile used in the simulations is the same as that used in the experiments. Readers are encouraged to refer to the companion work for more information on the experimental set-up (Alva *et al.* 2023). Here, a brief summary of the geometry and flow conditions is presented.

The geometry investigated here is a modified NACA 0012 airfoil. The airfoil has a zero angle of attack and the free-stream Mach number is set to be $M = U_\infty/a_\infty = 0.3$, where U_∞ is the free-stream velocity and a_∞ is the free-stream speed of sound. Two values of the Reynolds number, 0.8×10^5 and 1.0×10^5, have been chosen to be investigated for potentially different flow phenomena. The chord length of the model is $c = 100$ mm. Unlike the theoretical NACA 0012 profile, the trailing edge is truncated at around 98 % of the chord length and rounded with an arc-circle of radius $0.04c$, in order to control the trailing-edge shape, in agreement with earlier works of Ricciardi *et al.* (2022) and Ricciardi & Wolf (2022). The boundary-layer displacement thickness at the trailing-edge location is expected to be much thicker than the trailing-edge thickness. Thus, trailing-edge bluntness is not expected to be dominant for trailing-edge noise (Brooks *et al.* 1989).

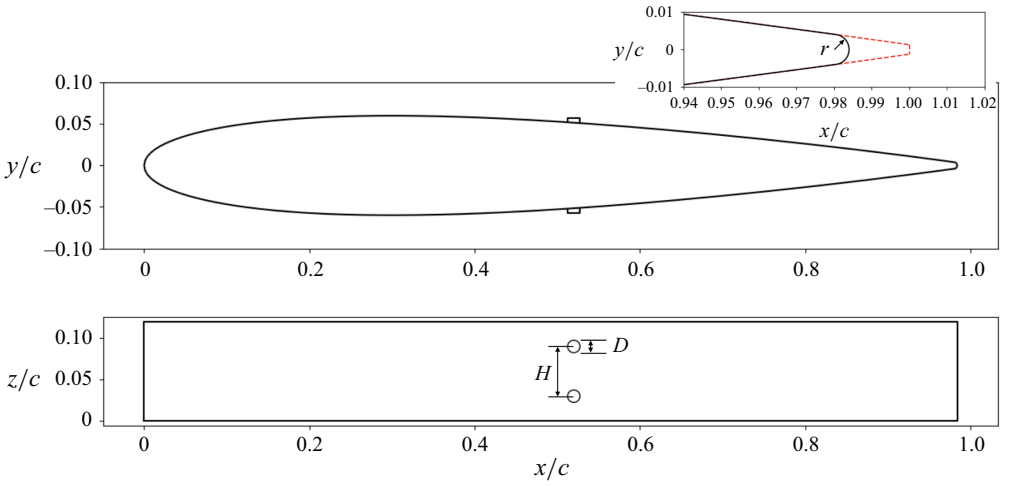

Figure 1. A schematic drawing of the modified NACA 0012 airfoil with roughness elements. The roughness elements are located at $x = 0.52c$ with a diameter of $D = 0.015c$. The distance between the elements is $H = 0.06c$. The red dashed line indicates the original NACA 0012 airfoil profile. The modified NACA 0012 profile is truncated at $x = 0.98c$ and rounded with an arc of radius $r = 0.04c$.

In the present study, we consider two different geometries: one with a smooth surface and one with a row of spanwise-periodic roughness elements on both sides of the airfoil. The choice of roughness elements follows the work of Fransson *et al.* (2005). The roughness elements have a height of $0.0055c$ (around 0.3 boundary-layer thickness) and a diameter of $0.015c$. The distance between them is $0.06c$. These roughness elements are placed close to the mid-chord position, at $x/c = 0.52$.

The extension of the computational domain in the spanwise direction is $0.12c$, which contains two periods of roughness elements. A periodic boundary condition is used in the spanwise direction. According to the scattering condition, in order to generate propagating acoustic waves, the spanwise wavenumber has to satisfy $k_z < k_0$, where k_0 is the acoustic wavenumber (Nogueira, Cavalieri & Jordan 2017; Sano *et al.* 2019; Demange *et al.* 2024*b*; Yuan *et al.* 2024). In this study, spanwise-coherent two-dimensional flow structures ($k_z = 0$) dominate the generation of tonal noise. Therefore, the choice of the spanwise width is expected to have a reduced effect on the noise generation. A schematic drawing of the modified airfoil profile is shown in figure 1.

2.2. *Numerical methods*

The open-source high-order flux-reconstruction numerical framework PyFR (Witherden, Farrington & Vincent 2014) is used for wall-resolved implicit LES (iLES) to solve the compressible Navier–Stokes equations in the general Cartesian coordinates with geometries stated above. Unlike LES with subgrid-scale models, iLES introduces numerical dissipation by discretisation. In this simulation, we use an anti-aliasing technique via the approximate L^2 projection, which has proven to be numerically stable and efficient. The principle behind this anti-aliasing is to compute the modal expansion coefficients of the desired polynomial exactly; see Park, Witherden & Vincent (2017) for details. The discrete set of equations obtained from the spatial-spectral (hp)-type discretisation is integrated in time using a total variation diminishing third-order Runge–Kutta method. The simulations are performed using fourth-order polynomials.

In this work, the length scales, velocity components, density, pressure and frequency are non-dimensionalised as $x = x^*/c$, $u = u^*/a_\infty$, $\rho = \rho^*/\rho_\infty$, $p = p^*/(\gamma a_\infty^2 \rho_\infty)$ and $St = f^* c/U_\infty$, respectively. Here, ρ_∞ is the free-stream density, γ is the specific heat ratio and the quantities with the superscript $*$ are given in dimensional units. Therefore, the frequency St presented here is a Strouhal number. Furthermore, Sutherland's law is applied for the viscosity correction.

All simulations are performed on LUMI-G AMD MI250X 128 Gb GPU nodes. A compressible Navier–Stokes solver of fourth-order polynomials with hip-backend is used. The quadrature order used in the simulation is one order higher than the solver's polynomial order to fit the requirement of iLES (Park *et al.* 2017). Interior solution points (i.e. Gauss–Legendre points for the hexahedral elements) are used for anti-aliasing purposes. Furthermore, at least 2800 snapshots (around 84 flow overs) are taken for all cases for spectral analysis. At least 30 flow overs are discarded before collection of snapshots. Around 4000 GPU hours are consumed for each case.

2.3. *Mesh presentation*

PyFR supports both structured and unstructured mesh topology. To take advantage of this, we used the following meshing strategy. A wall-resolved O-grid with maximum resolution at around mid-chord is given by $\Delta x^+ < 20$, $\Delta z^+ < 10$, $\Delta y^+ < 0.9$, in a region where the flow is basically laminar. The $+$ superscript denotes viscous units. Considering that the flow on the airfoil is still transitional or fully developed to turbulence in the high-*Re* cases, at the trailing edge the resolution in the streamwise and wall-normal directions is kept as $\Delta x^+ < 4$, $\Delta y^+ < 0.7$. Near-wall mesh elements are lifted to second order to accommodate geometry curvatures. The structured mesh is also applied in the wake-resolved region until $1.5c$ after the trailing edge. The first layer of elements from the airfoil surface has an initial height of $\Delta y = 0.00055c$ and the growth rate of the structured layers is 1.08. For the cases with roughness elements, a prism type of mesh is applied in the near-roughness region to have a better fit of the roughness shapes and to avoid stretching of the mesh. The prism layer has much smaller elements with $\Delta s = 0.002c$ in the streamwise direction, which can reduce mesh-to-mesh discontinuity due to the discontinuous nature of the flux-reconstruction method.

In the acoustic region, unstructured grids are applied to reduce the large aspect ratio and significantly reduce the computational cost. Analysis of the simulation data shows that acoustic waves are still resolved up to Strouhal number $St = 15$. The element aspect ratio in this region is kept below 5. Meshing details are shown in figure 2. The total grid number is around 70 million (polynomial order of 4). To allow a proper representation of the acoustic field and to have less interference from boundary conditions to the airfoil, the computational domain has been extended to 15 chords away from the airfoil surface. A designed sponge zone is added around the outer boundaries to absorb hydrodynamic wake and acoustic waves (Freund 1997; Bodony 2006). The sponge is added as a forcing term $-\sigma(q - q_0)$ to the solver. Here, q_0 denotes free-stream quantities in the conservative format and the sponge strength parameter $\sigma = 0.008$ is carefully chosen such that flow solutions are damped to free-stream values. At the outflow boundaries we apply the non-reflective Riemann-invariant boundary conditions, which creates the outflow boundary conditions with free-stream values, together with the sponge zones, minimising reflections at the boundaries. At the inflow boundary, the Riemann-invariant condition is also used to provide a homogeneous potential flow with $M = 0.3$. A periodic boundary condition is used in the spanwise direction. A non-slip adiabatic wall condition is applied to the airfoil surface.

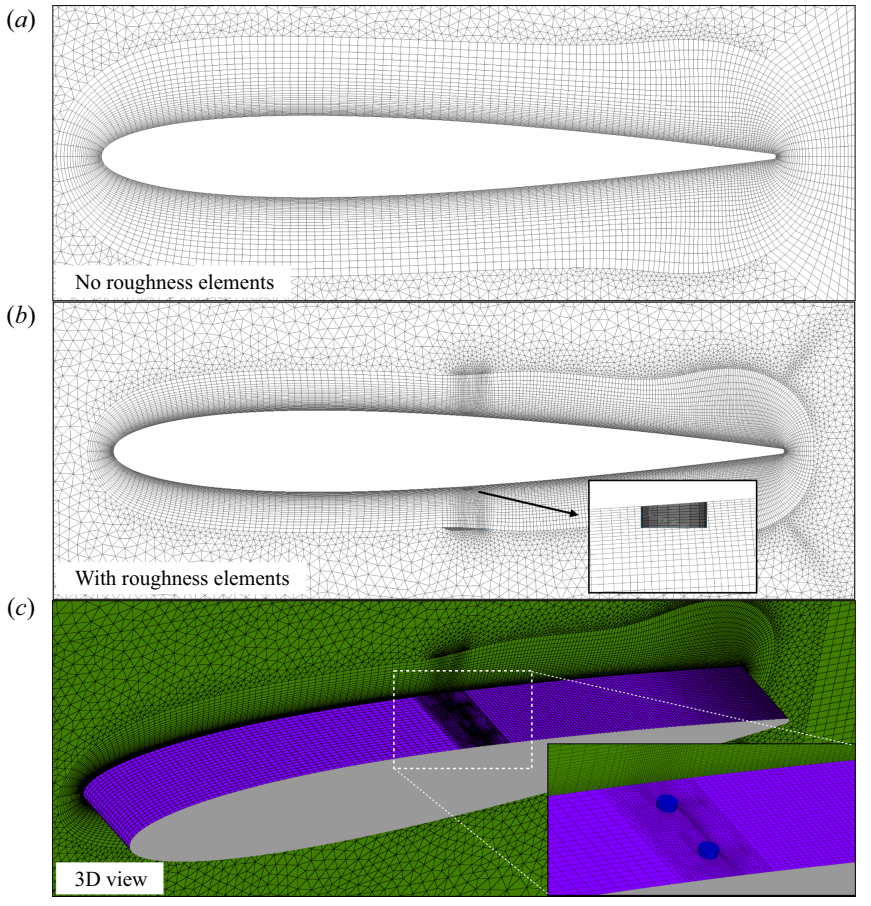

Figure 2. High-order computational mesh elements (polynomial order of 4) near the airfoil (*a*) without roughness elements (clean case) and (*b*) with roughness elements (rough case). (*c*) Three-dimensional view of the wall surface mesh with roughness elements. Grid points inside the elements are skipped for a better visualisation. Structured grids are applied in the near-wall region, while unstructured grids are applied in the acoustic region.

2.4. *Mesh validation*

The mesh of the current simulation is designed targeting at the higher Reynolds number, i.e. $Re = 1\,00\,000$. The mesh has a distribution of points in the streamwise and spanwise directions on the airfoil surface given by $n_x = 830$ and $n_z = 130$, respectively. From the airfoil surface to the height of the roughness elements ($\triangle h = 0.0055c$), the distribution of points in the wall-normal direction is given by $n_y = 45$. For clarification, we name this mesh as $M0$ which has a total of 4.86 million grid points in this near-wall region. A refined mesh $M1$ is designed as $n_x = 1185$, $n_y = 50$ and $n_z = 170$ which leads to 10.07 million grid points in the near-wall region. The refinement is more concentrated from the roughness elements to the trailing-edge region where the flow gradients introduced by flow transition are much larger. Moreover, the aspect ratio is maintained. In the end, $M0$ leads to 70 million and $M1$ results in 80 million grid points in the computational domain.

Figure 3 illustrates a comparison between two mesh designs. Velocity profiles are acquired at the streamwise locations $x/c = 0.85$ and $x/c = 0.95$. The velocity profiles show great convergence as overlapping for both mesh designs. The spectrum of the wall

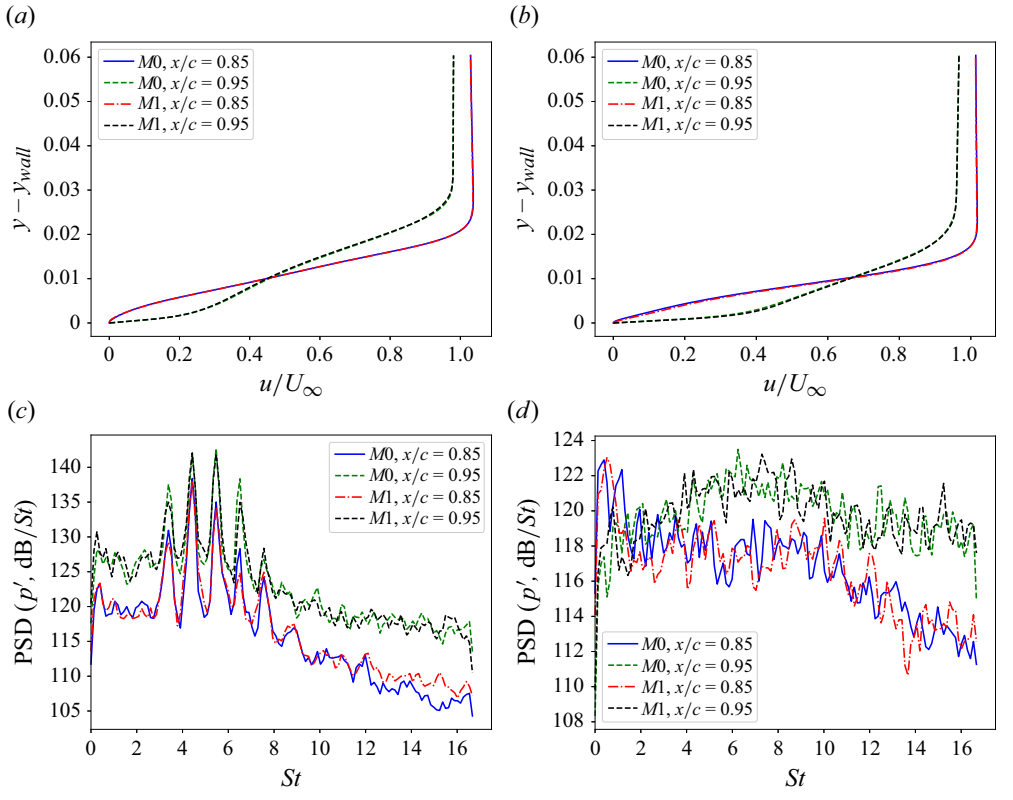

Figure 3. Mesh refinement study. Mean flow profiles measured for roughness cases at $x/c = 0.85$ and $x/c = 0.95$ with (*a*) $Re = 80$k and (*b*) $Re = 100$k. The wall pressure spectrum obtained at $x/c = 0.85$ and $x/c = 0.95$ for (*c*) $Re = 80$k case and (*d*) $Re = 100$k case.

pressure signal is presented in figures 3(*c*) and 3(*d*) at the same locations and for the rough cases of both Reynolds numbers. Both mesh set-ups are able to capture the tonal peaks and secondary tones at $Re = 80$k and give the same broadband trend as for the high-Reynolds-number case. There are slight differences due to the fact that the time series acquired for the $M1$ mesh is shorter than that for the $M0$ mesh. For the case without roughness elements, the flow around the airfoil is expected to display weaker gradients, such that our mesh resolution $M0$ is more than sufficient. Note that both mesh set-ups use fourth-order polynomials and h-type refinement is carried out. Since our cases are performed with iLES with anti-aliasing via projection acting on the surface flux (Park *et al.* 2017), p-type refinement, i.e. increasing the polynomial order, will lead to a change in the filter as well as a change in the effect of the filter caused by the time scheme. Thus, p-type refinement with the LES filter for grid convergence study is not considered in this study. The data computed from $M0$ are employed in the following data analysis.

3. Simulation results

3.1. *Acoustics*

In order to compare with the experimental results, the power spectrum density (PSD) of the pressure fluctuations at the location $x/c = y/c = 1$ is illustrated in figure 4. The origin is taken at the leading edge of the airfoil, and this location is thus at 90° from the

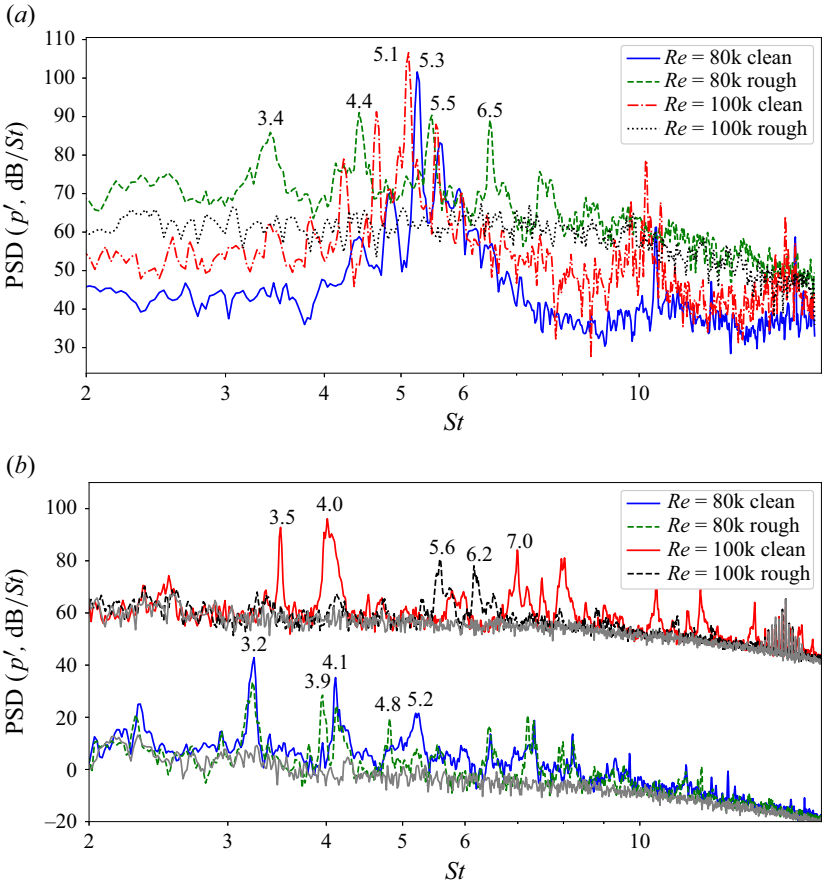

Figure 4. Acoustic spectra for (*a*) numerical simulations and (*b*) experiments measured in dB/*St*. In (*b*), results of $Re = 80$k cases are shifted 55 dB lower for better visualisation. Tonal frequencies are labelled. Grey line: wind tunnel background noise.

trailing edge. In the experiments, a beamforming technique is applied to compute the PSD of the pressure fluctuation, and a detailed description can be found in the experimental part of this work (Alva *et al.* 2023). A Welch method (Welch 1967) is used to calculate the PSD. For the LES data, the segment length of the Fourier transform is 512 and the overlap percentage is set to 75 %, which results in 22 blocks. The length of the time signal is 90 flow overs (c/U_∞) with sampling frequency $St = 33.3$ to ensure a well converged dataset. Results are presented here in terms of the sound pressure level, which is defined in decibels (dB) as

$$L_p = 10 \log_{10} \frac{P_{xx}}{p_0^2} \tag{3.1}$$

with a reference sound pressure $p_0 = 2 \times 10^{-5}$ Pa; we denote the PSD of the pressure fluctuations by P_{xx}. Furthermore, the acoustic Mach number scaling (Williams & Hall 1970; Brooks & Marcolini 1985), i.e. M^5, is applied to the numerical dataset. This scaling helps to match the tonal acoustic amplitude from both the numerical and experimental datasets.

For all numerical clean cases, the spectrum is dominated by a main frequency of $St = 5.5$ for the $Re = 80$k clean case and $St = 5.2$ for the $Re = 100$k clean case. As the Reynolds number increases, the main tone shifts to a slightly lower frequency but it has a stronger tonal noise amplitude. It is evident that secondary tones emerge in the spectrum at frequencies slightly lower and higher than the primary tone. As suggested by Tam (1974), the combination of the primary tone and the secondary tones is also referred to as ladder-like structures. With roughness elements being added to the airfoil surface, the main tone in the $Re = 80$k case has been broken down into multiple tones with much lower amplitude and wider frequency bands. Those tones have more or less similar amplitudes, and it becomes harder to distinguish a primary tone in the spectrum. In the $Re = 100$k rough case, the spectrum becomes broadband. Both the main tone and secondary tones are eliminated. The overall sound pressure level (OASPL) is calculated by integrating the spectrum in figure 4(*a*). The OASPL decreases from 89.1 to 85.6 dB in the case of $Re = 80$k and from 94.1 to 72.8 dB in the case of $Re = 100$k, from the clean to rough geometry, respectively. The OASPL results show that in the case of $Re = 80$k, the acoustic energy is redistributed to tones with lower amplitude, but with an overall decrease of about 3 dB. In the case of $Re = 100$k, the decrease of the main tones leads to a large overall reduction in noise.

Figure 4(*b*) presents the experimental measurement of the acoustic spectrum. A direct comparison between simulation and experiment is not possible, as is discussed later, but similar trends appear. For visualisation purposes, the results for $Re = 80$k cases are shifted 55 dB lower. For $Re = 80$k cases, both clean and rough surfaces can generate tonal noise. For the clean geometry the main tones have frequency $St = 3.2$ and $St = 4.1$. The noise level for the rough case is lower and the peak frequency is shifted away from that of the clean case. More tones can be observed at higher frequencies, i.e. $St = 3.1$, 3.9 and 4.8. For the $Re = 100$k cases, very strong tonal noise can be observed at $St = 3.5$, 4.0, 7.0 and 8.0 for the clean geometry, while most of the tones are eliminated from the spectrum with the presence of roughness elements, with the exception of tones at $St = 5.6$ and 6.2 with much lower amplitudes.

Accounting for a Mach number scaling following M^5 (Williams & Hall 1970; Brooks & Marcolini 1985), the tonal amplitudes between the numerical and experimental results are comparable, namely around 100 dB for case $Re = 100$k clean, 97 dB for case $Re = 80$k clean and 91 dB for case $Re = 80$k rough. The difference between the simulation and experimental results is within 3 dB. However, the tonal frequencies in the two datasets differ. This is likely for a number of reasons. First, in the simulation, free-stream turbulence (FST) level is assumed to be zero. However, this FST can lead to early transition to turbulence which eventually can affect the noise generation. Second, the experiments are carried out in a closed-section wind tunnel, unlike the free-field conditions used in the simulation. Finally, and perhaps more significantly, there is a Mach number difference between experiments and simulations (Mach = 0.3 in numerical simulations and Mach = 0.037 for experiments). In the experimental work of Pröbsting (2022), the authors found that at zero incidence the tonal noise regime in the low-to-moderate Reynolds-number regime is sensitive to the variation in Mach number. The authors used the theoretical model from Arbey & Bataille (1983) and successfully predicted the tonal noise frequency intervals experimentally. In Appendix A, we employ the same analysis and find that both numerical and experimental datasets follow Arbey and Bataille's model. Furthermore, we also perform the simulation with $M = 0.1$ and $Re = 80$k. The results are presented in Appendix B and the results show the relation of dominant tonal frequency and the

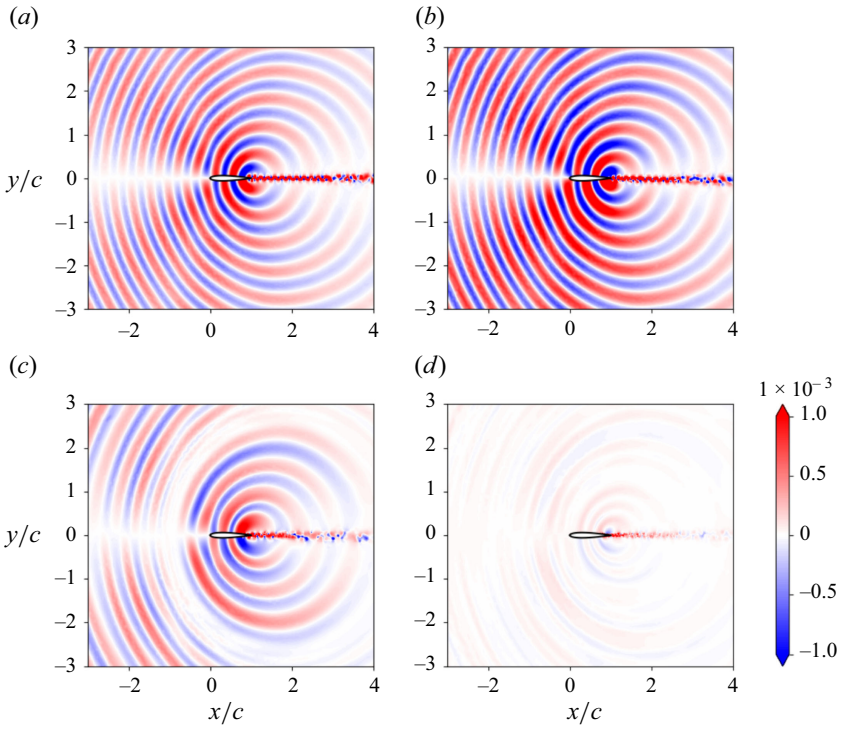

Figure 5. Acoustic field contour plots for pressure fluctuation p'. The airfoil leading-edge point is at $x/c = y/c = 0$. (*a*) $Re = 80$k clean, (*b*) $Re = 100$k clean, (*c*) $Re = 80$k rough and (*d*) $Re = 100$k rough.

Mach number, which follows the findings of Ricciardi, Arias-Ramirez & Wolf (2020) and Pröbsting (2022). The influence of the FST is discussed in Appendix C which shows the limited influence on the results with low turbulence intensity (TI = 0.16 %) as in the experiments. In this work, we did not intend to match the experiments exactly due to the cost of the simulations. However, it is already encouraging that the same qualitative trends related to the use of roughness elements are observed in both simulation and experiment.

Sample snapshots of the two-dimensional acoustic fields of all four cases are illustrated in figure 5 with pressure fluctuation p'. In the clean cases, strong acoustic radiation can be observed from the trailing-edge region. From lower to higher Reynolds number, the amplitude of the acoustic waves becomes stronger. With the presence of roughness elements, the amplitude of acoustic waves is lower and the wavelength is changed compared with the clean cases. For $Re = 100$k rough case, the acoustic radiation is much lower than for other cases and it is hard to identify under the same level range. These observations are consistent with the results of the acoustic spectra in figure 4.

The directivity of cases $Re = 80$k clean/rough and $Re = 100$k clean are presented in figure 6. The directivity is obtained along an arc-circle with the origin at the trailing edge and radius of $2c$, and wake region is excluded. The directivity corresponding to the tonal frequencies is presented. Similar to Demange *et al.* (2024*a*), the directivity of the tonal frequencies shows as a modified cardioid pattern, arising from interferences between trailing- and leading-edge scattering (Howe 2001; Roger & Moreau 2005).

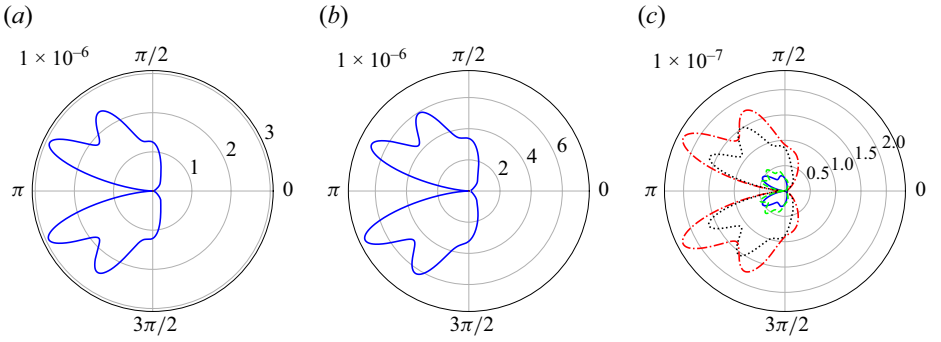

Figure 6. Directivity plots of the acoustic field for (*a*) $Re = 80$k clean, $St = 5.3$ (——), (*b*) $Re = 100$k clean, $St = 5.1$ (——) and (*c*) $Re = 80$k rough, $St = 3.4$ (——), $St = 4.5$ (- - -), $St = 5.5$ (·····), $St = 6.5$ (- - -).

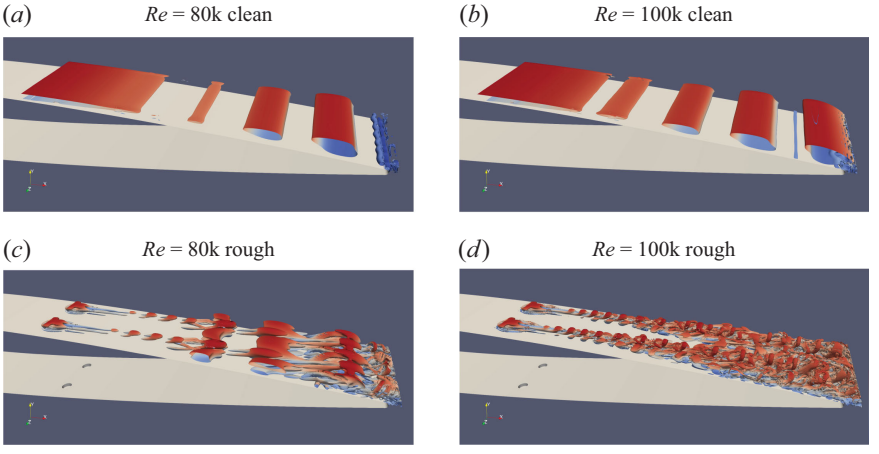

Figure 7. Iso-surface of the Q-criterion coloured by streamwise velocity u.

3.2. *Flow structures*

As an overview of the flow structures, the visualisation of the flow field is presented in figure 7 in terms of the Q-criterion (Jeong & Hussain 1995) coloured by the streamwise velocity component u. The Q-criterion is defined as $1/2(||R||^2 - ||S||^2)$, where R and S are the rotation and strain rate tensors, respectively. To enhance visualisation and conserve computational resources, a boxed region covering the upper side of the airfoil is utilised for calculating the Q-criterion. The Q-criterion can help us to identify the flow states and dominant structures on the airfoil. The Q-criterion values used in the visualisations for the clean cases are one order of magnitude higher than those for the rough cases. Videos corresponding to four cases can be seen as supplementary movies available at https://doi.org/10.1017/jfm.2025.10321.

For clean cases, the dominant structures are K–H-type rollers. These spanwise-coherent structures are responsible for the tonal noise generation at the trailing edge as also identified in the works of Pröbsting *et al.* (2015) and Ricciardi *et al.* (2022). With roughness elements being added to the airfoil surface for both Reynolds numbers, streaky structures are generated by these roughness elements. These streaks will develop into lambda structures (also called hairpins) while propagating downstream and modulating K–H rollers. At the lower *Re*, K–H-type rollers are modulated but maintain a certain level

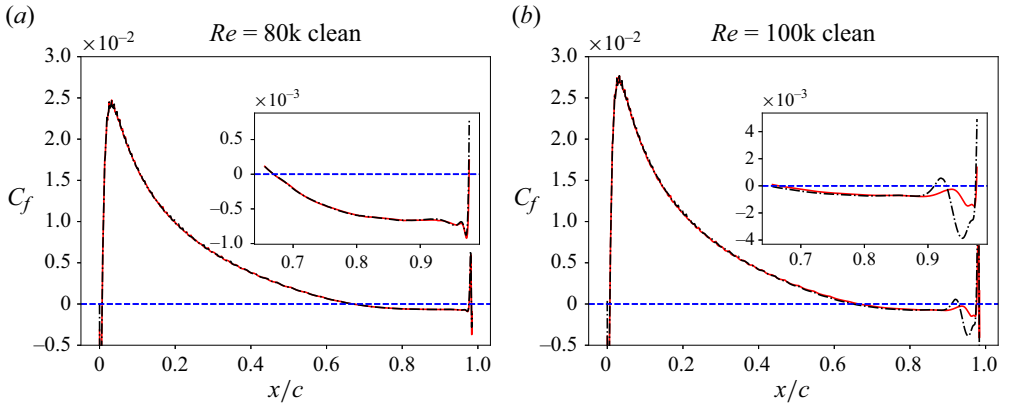

Figure 8. Skin friction coefficient (C_f) of span-averaged field of the clean cases at both Reynolds numbers: (*a*) $Re = 80$k; (*b*) $Re = 100$k. Solid red line and dashed black line represent upper and lower sides of the airfoil, respectively. Blue dashed line indicates zero values.

of spanwise coherence. An earlier breakdown of the K–H rollers to three-dimensional structures is spotted close to the trailing edge. With an increase of *Re*, the flow structure on the airfoil surface becomes dominated by three-dimensional lambda structures. The trace of spanwise-coherent structures is very weak. From these observations, we can infer that these structures may link the acoustic field presented in figure 4 and the hydrodynamic field. Tonal noise is generated by a feedback mechanism involving the spanwise-coherent K–H rollers. The streak-modulated K–H rollers have lower spanwise coherence, which ultimately decreases the acoustic amplitude and shifts the tonal frequencies. Stronger streaks at higher *Re* could lead to an earlier breakdown to three-dimensional structures which will generate broadband type of noise rather than tonal noise. Further analysis of these aspects is presented in § 4.

In the numerical work of Ricciardi *et al.* (2022), separation bubbles play an important role, as they lead to strong K–H instabilities. In order to reveal the changes of the separation bubble induced by streaks, the span- and time-averaged skin friction coefficients (C_f) for clean cases are shown in figure 8. Here the skin friction coefficient is defined as

$$C_f = \frac{\tau_w}{0.5\rho_\infty U_\infty^2}, \tag{3.2}$$

where τ_w represents the wall shear stress and subscript ∞ refers to the free-stream quantities. For the clean cases, a long separation bubble can be spotted on the both sides of airfoil. At $Re = 80$k, the separation bubble initiates at $x/c = 0.65$ and at $x/c = 0.67$ for the higher-*Re* case, extending up to the trailing edge. A significant difference of C_f at the two sides of airfoil close to the trailing edge can be seen for the higher-*Re* case. This phenomenon has also been documented in the work of Ricciardi *et al.* (2020) where a series of two-dimensional simulations were conducted at low Reynolds numbers and Mach numbers. At $Re = 100$k and Mach $= 0.3$, the dynamics displays symmetry breaking, with a stronger separation bubble at one of the airfoil sides which occasionally switches to the other side. Apparently, our dataset does not cover such a long time evolution, which could be the reason for the difference of C_f between the two sides of the airfoil. Though this could slightly affect the tonal noise characteristics, it does not change the fact that streaks can attenuate the tonal noise level. And as discussed in the following analysis, with the presence of the streaks, the C_f distributions of both sides of the airfoil are identical. So in

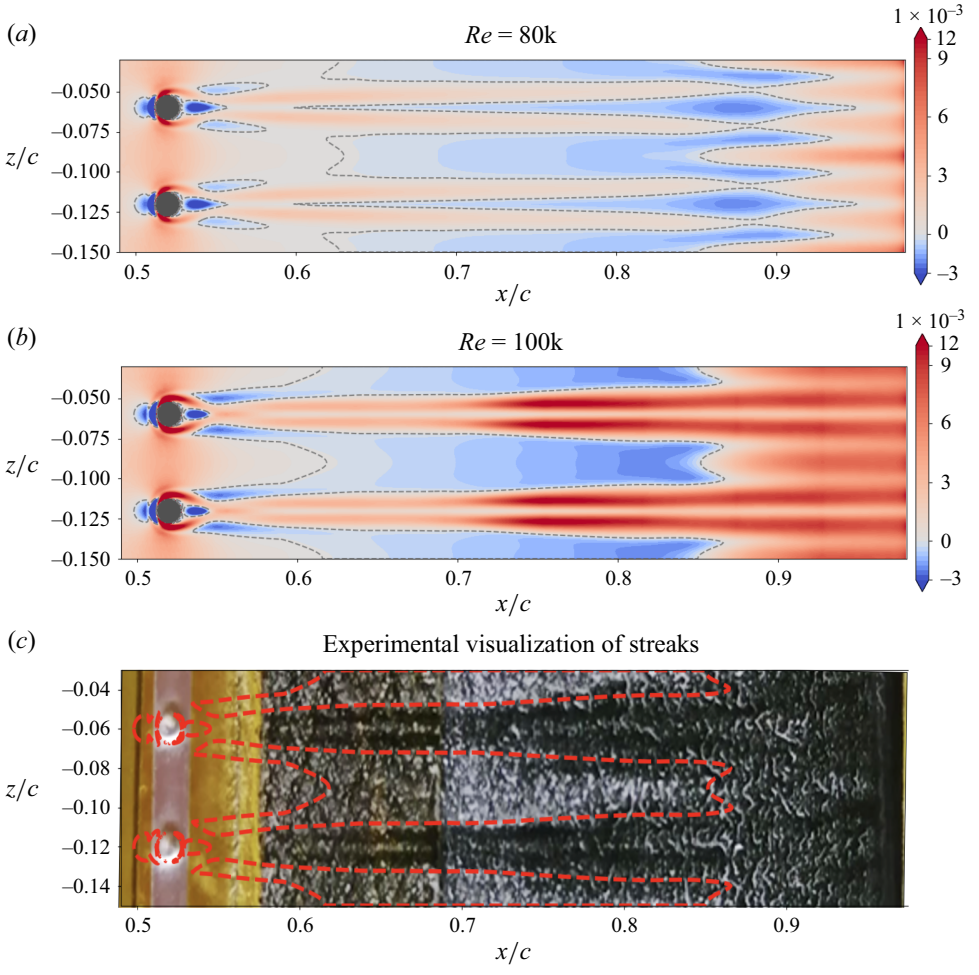

Figure 9. (*a*,*b*) Skin friction coefficient (C_f) heat maps of mean flow field of roughness cases. Red is positive and blue is negative. Dashed grey line is zero-contour line. (*c*) Oil visualisation from the experimental campaign at $Re = 1\ 50\ 000$. Red dashed line: the zero-contour line from $Re = 100$k simulation projected on the oil visualisation.

order to avoid long and expensive simulations to have fully converged statistics, we keep the current dataset for further analysis.

For the cases with roughness elements, the structures on the airfoil are three-dimensional. Hence, spanwise-averaged statistics are no longer appropriate. Thus, to understand how the existence of structures generated by the roughness elements modifies the surface flow field, the time-averaged surface skin friction coefficient heat maps are presented in figure 9(*a*,*b*). The colour map is saturated such that blue indicates negative and red represents positive values. The grey dashed line indicates the zero-contour line. A re-circulation region can be spotted prior to and after the cylinder roughness in both cases. Downstream of the location of the roughness elements, a long separation bubble (characterised by negative C_f regions) can be spotted in both cases. However, the separation bubble has been sliced/modulated into subdomains by the streamwise-elongated structures highlighted by the positive C_f values. Fast streaks (indicated by regions of positive C_f) are induced downstream of roughness elements,

in agreement with earlier studies (Fransson *et al.* 2004, 2005). At lower Reynolds numbers, streaks have significantly lower amplitudes. The initial locations of separation bubbles are roughly equivalent to those in the clean case, yet the re-attachment location is further upstream compared with the clean case. For the high-*Re* case, streaks have higher amplitude immediately after the roughness elements, maintaining it until the trailing-edge region. The end of the separation bubble moves upstream, to around $x/c = 0.86$.

Figure 9(*c*) illustrates flow visualisation from the experiment at $Re = 1\ 50\ 000$ in which the surface oil flow visualisation technique is employed to reveal flow patterns, with technical details provided in the companion paper. It should be noted that a higher-Reynolds-number case is presented to enhance the visualisation effect, as lower-speed flows did not lead to clear visualisations in the wind tunnel. The overall mechanism remains the same: this visualisation method captures the fast and slow streaks directly behind the roughness elements, with streak traces extending up to around $x/c = 0.9$. This finding is highly consistent with the C_f distribution from the simulation depicted in the same figure. The zero-velocity contour line from the simulation $Re = 100$k case is projected to the oil visualisation and, clearly, the location and width of the streaks are very similar in both cases.

4. Spectral and stability analysis

The observations mentioned above confirm the presence and significance of streaks in modulating spanwise-coherent structures, ultimately leading to a reduction in tonal noise. In this section, we use data-driven spectral and local stability analysis methods to quantify the contribution of streaks in reducing the growth of spanwise-coherent structures. In order to accomplish this, a series of cross planes at different streamwise locations ($x/c = 0.55$, 0.65, 0.75, 0.85, 0.95) are used for the analysis. The local coordinates used here are $z - z'$ and $y - y_w$, where z' represents the centre of the cylinder roughness and y_w is the wall location. Results with respect to only one period of cylindrical roughness element are presented in the following context.

The wall-tangential mean-flow profile u_t at these locations is shown in figure 10. Here u_t is defined as the difference between the time-averaged mean profile and the time-spanwise mean profile as an indication of the modification of the mean flow by streaks. In addition, arrow fields generated by the time-averaged wall-normal and spanwise velocity components (v, w) are added to the contour plots to help identify streamwise vortices. The amplitude of the contours and arrows is kept the same across all stations for better comparison.

At the station close to the roughness elements ($x/c = 0.55$), the arrow field plot clearly reveals a pair of counter-rotating vortices that transport high-velocity fluid from the free stream downward to the near-wall region and low-velocity fluid from the near-wall region to the high momentum fluid region. This phenomenon is commonly referred to as the 'lift-up' effect mechanism, as detailed by Ellingsen & Palm (1975) and Landahl (1980) and more recently in the review by Brandt (2014). Through the lift-up mechanism, a low-velocity streak appears further away from the wall, along the centreline of the roughness element and high-speed streaks appear closer to the wall. As one moves towards the downstream stations, we see the emergence of counter-rotating streamwise vortices, which are responsible for the central low-speed streak that develops downstream. Furthermore, the streamwise vortices start to spread in the spanwise direction and their amplitude decreases. For the higher-*Re* case, the overall mechanisms are the same, but more pronounced streaks are present, leading to stronger evidence of fluid

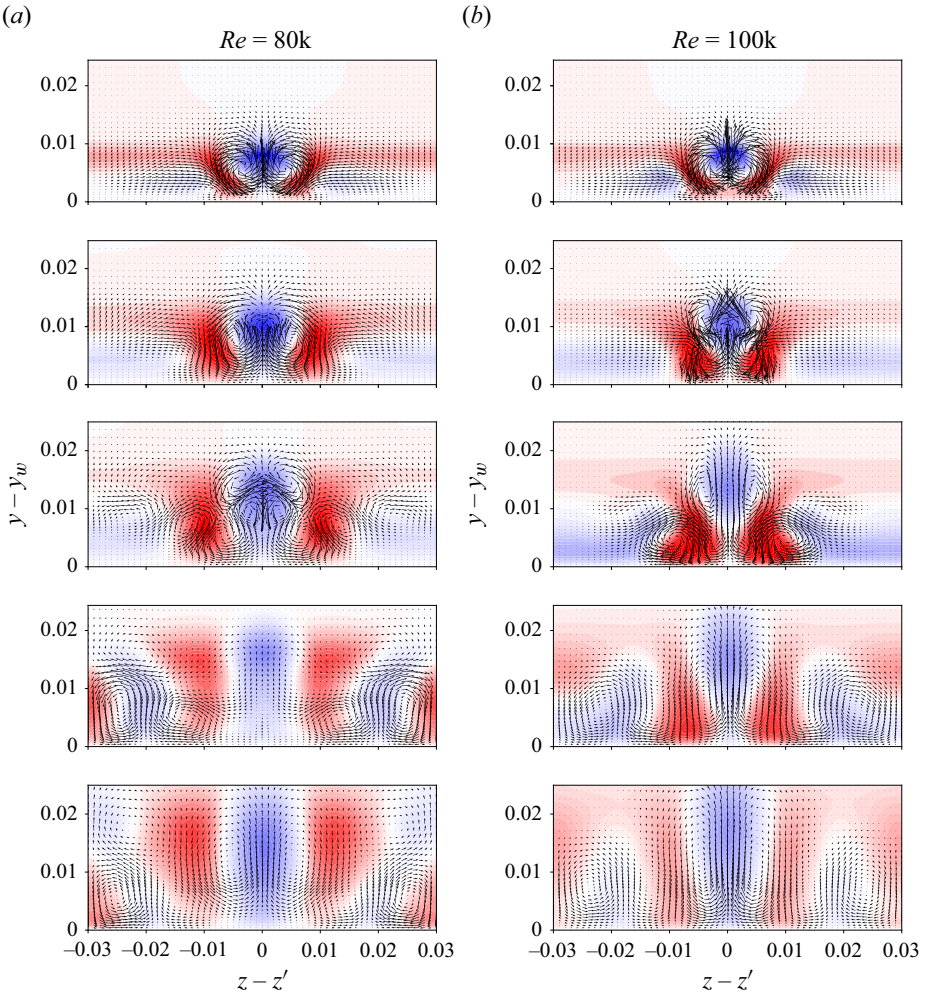

Figure 10. Contour plots show the wall-tangent mean flow u_t, where u_t indicates the difference between the time-averaged and time-spanwise-averaged wall-tangent mean flow. Contour level range $u_t/U_\infty \in [0, 0.18]$. Arrow fields show time-averaged velocity components v and w in the wall-normal and spanwise directions, respectively. From top to bottom, the rows show streamwise stations $x/c = 0.55, 0.65, 0.75, 0.85, 0.95$.

transport. This can be seen at $x/c = 0.75$, where the $Re = 100$k case shows that high-momentum fluid occurs much closer to the wall region compared with the lower-Re case. Through the lift-up mechanism, the reverse flow is counteracted by high-speed fluid as shown in figure 9.

4.1. *Spectral proper orthogonal decomposition*

The previous visualisations are of steady structures induced by the roughness elements. We now characterise fluctuating fields, which are expected to be directly related to acoustic radiation, using modal analysis. The POD technique is a data-driven method which extracts a set of orthogonal basis functions from flow realisations (Lumley 1970; Berkooz, Holmes & Lumley 1993) that maximise the mean square energy, considering an appropriate inner product. In SPOD (Picard & Delville 1999; Towne, Schmidt & Colonius 2018), this basis is defined by the eigenvalue decomposition of the cross spectral density matrix of the

Fourier-transformed realisations at each frequency, ensuring spatio-temporal coherence of the structures. We consider the standard Reynolds decomposition of the flow variables, i.e. $q = \bar{q} + q'$, where $\bar{q} = [\overline{\rho}, \overline{u}, \overline{v}, \overline{w}, \overline{T}]^{\mathrm{T}}$ stands for the time average and q' is the fluctuation component. Here in this work, we define the fluid component as $q' = [\rho', u', v', w', T']^{\mathrm{T}}$ as the density, tangential, wall-normal and spanwise velocity components and temperature fluctuations, respectively. Since SPOD is applied to compressible flow components at the streamwise cut locations, the norm used here is the compressible energy (Chu 1965; Mack 1984; Hanifi, Schmid & Henningson 1996). Following the so-called snapshot method (Schmidt & Colonius 2020), firstly a windowed fast Fourier transform is performed on the fluid field data in time to obtain the flow field $\hat{q}$ (where a hat denotes a Fourier-transformed quantity) at each discrete frequency. The decomposition is performed at each frequency based on the inner product between different flow realisations $\hat{q}_i$, given by

$$\langle \hat{q}_i, \hat{q}_j \rangle = \int_{\Omega} \hat{q}_j^H \mathcal{W} \hat{q}_i \, \mathrm{d}\mathbf{x} = \hat{q}_j^H \mathbf{W} \hat{q}_i, \tag{4.1}$$

where Ω is the region of interest, the superscript H denotes the Hermitian transpose and the discretised weighting operator, $\mathbf{W}$, is chosen such that the sum of the eigenvalues defines a compressible energy (related to the variance of the cross spectral density). Following the original derivation from Chu (1965), $\mathbf{W}$ is a positive-definite weighting tensor:

$$\mathbf{W} = \int_{\Omega} \begin{bmatrix} \frac{\overline{T}}{\gamma \overline{\rho} M^2} & & & & \\ & \overline{\rho} & & & \\ & & \overline{\rho} & & \\ & & & \overline{\rho} & \\ & & & & \frac{\overline{\rho}}{\gamma(\gamma-1)\overline{T}M^2} \end{bmatrix} \mathrm{d}\mathbf{x}, \tag{4.2}$$

where γ is the specific heat ratio and M is the Mach number.

In all the analyses studied here, we have used Hamming windows for the Welch method, since they are commonly used in narrowband applications. The analysis is performed with the numerical code from Schmidt & Colonius (2020), using a short-time fast Fourier transform considering $N_{FFT} = 128$ frequency bins per block with an overlap of 75 %, resulting in a number of blocks $N_{blocks} = 172$ and $\Delta T = 0.03c/U_{\infty}$. In order to increase the resolution of SPOD analysis, data from the two periods of roughness elements on one side of the airfoil are treated as two independent realisations. As the case with roughness elements does not allow a Fourier transform along the spanwise direction, SPOD modes have a non-trivial z dependency. To limit the data requirements, we apply SPOD separately at the streamwise positions illustrated in figure 10.

The energy spectrum (γ_i) calculated at the station $x/c = 0.75$ is presented in figure 11 for both Reynolds numbers. At lower *Re*, a group of noticeable peaks can be observed in the spectrum at $St = 5.5$, 4.4 and 6.5. Those peaks in the spectrum are related to the tonal noise illustrated in the figure 4. As expected, for the higher *Re*, there are no clear peaks in the spectrum and no dominant frequency can be detected. In order to investigate the effects of roughness elements, we choose the frequency $St = 5.2$ in the $Re = 100$k case which corresponds to the tonal noise in the clean case. It is worthwhile to note that from the spectrum, the energy of the leading mode (γ_1) of chosen frequency is around one order of magnitude higher than that of the second mode (γ_2) at the frequencies of interest, which indicates that the system dynamics is of low rank, i.e. the flow is dominated by the first mode. The leading SPOD mode can thus be used as an effective representation for flow structures.

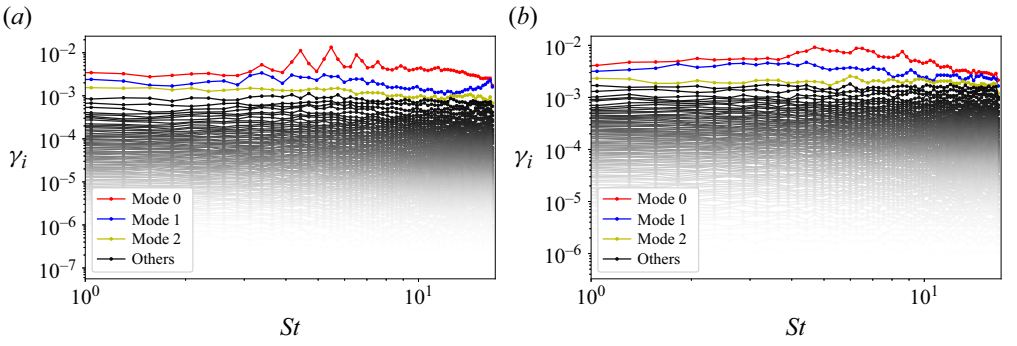

Figure 11. The SPOD energy (γ_i) calculated at the station $x/c = 0.75$ at $Re = 80$k (a) and $Re = 100$k (b). Data correspond to the rough cases.

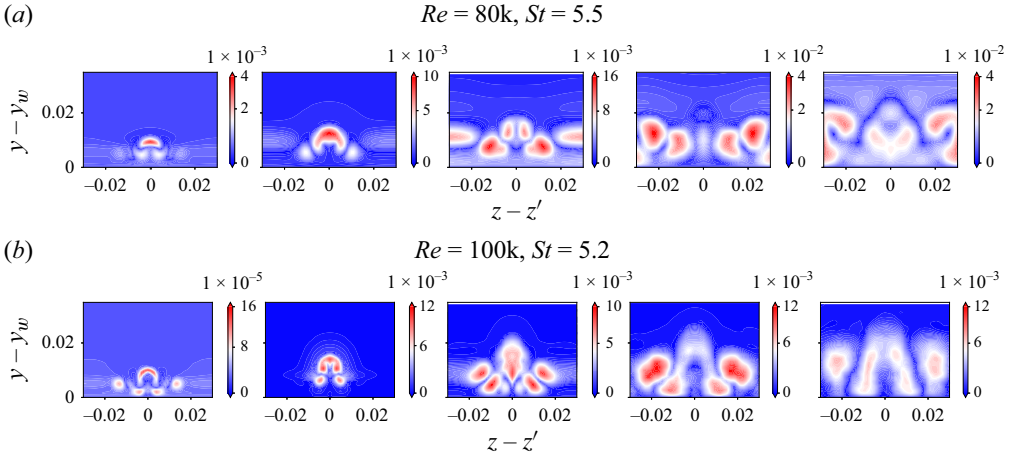

Figure 12. (a,b) Absolute value of the leading SPOD mode of streamwise velocity $\tilde{u}$. From left to right: stations $x/c = 0.55$, 0.65, 0.75, 0.85 and 0.95.

Figure 12 shows the absolute values of the leading SPOD mode of the wall-tangential velocities $\hat{u}$ at the selected streamwise stations. Note that SPOD modes have a unit norm, so to see the growth of structures at streamwise stations, SPOD modes are multiplied with the square root of the eigenvalue to show the actual fluctuation amplitudes in the flow. From the first and second stations ($x/c = 0.55$ and 0.65), we see the fast growth of the amplitude of unsteady streak-type structures with a change of almost two orders of magnitude for higher-Re case. At the station $x/c = 0.75$, for the lower-Re case, the growth of spanwise-modulated K–H rollers can be identified. Those structures sit at the location $|z - z'|/c \geqslant 0.015$. For the higher Re, similar patterns are observed. Although the spanwise coherence is lower for $Re = 100$k, the structures display patterns similar to those of the $Re = 80$k case, suggesting that, while of difficult identification in the Q-criterion snapshots, strongly modulated K–H rollers remain even for higher Reynolds numbers. From station $x/c = 0.85$ onward ($x/c \geqslant 0.85$), the amplitude of structures begins to decrease for the higher-Re case and continues to increase for the lower-Re case. With the growth of the boundary layer, flow structures start to spread out, marking the ongoing process of the transition to turbulence at these stations. Therefore, in the subsequent discussions, we primarily focus on the lower-Re scenario at around station $x/c = 0.75$.

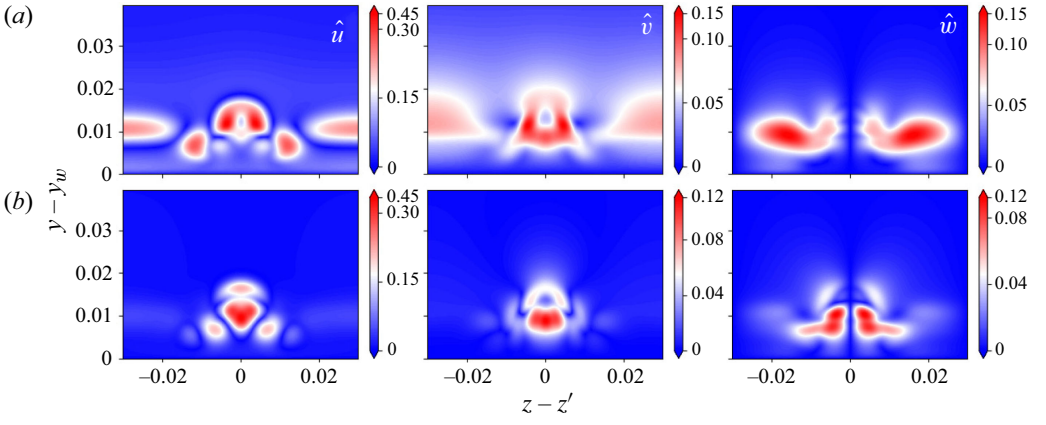

Figure 13. The absolute value of the leading (*a*) and secondary (*b*) SPOD modes calculated at the station $x/c = 0.75$ for $Re = 80$k. From left to right: velocity components $\hat{u}$, $\hat{v}$ and $\hat{w}$.

Figure 13 depicts the absolute values of the leading and secondary SPOD modes at $x/c = 0.75$ for $Re = 80$k. At this station, streaks are fully developed and the amplitudes of both streaks and K–H rolls have reached the same order of magnitude. From the figure, the leading SPOD mode describes a streak-modulated K–H roll, while the second mode contains only thinner localised structure akin to streak fluctuations. However, at this frequency, the flow field is dominated by the leading SPOD mode according to the energy ranking presented in figure 11. Hence, the leading SPOD mode is a good representation of the flow state. The most energetic structures are located $0.01c$ away from the airfoil surface.

4.2. *Local spatial stability analysis*

In order to investigate how the streaks attenuate growth of the K–H rolls, a two-dimensional spatial–local stability analysis in the $z-y$ plane is performed at the streamwise station $x/c = 0.75$. Here, we are interested in the analysis of the hydrodynamic part of the flow field, and because of the low Mach number of the flow, the incompressible linearised Navier–Stokes formulation is sufficient for the analysis:

$$\frac{\partial \mathbf{u}'}{\partial t} + (\bar{\mathbf{U}} \cdot \nabla)\mathbf{u}' + (\mathbf{u}' \cdot \nabla)\bar{\mathbf{U}} = -\nabla p' + \frac{1}{Re}\nabla^2 \mathbf{u}', \qquad \nabla \cdot \mathbf{u}' = 0, \tag{4.3}$$

where $\bar{\mathbf{U}}$ indicates the mean flow, upon which linearisation is performed and variables with primes indicate perturbation around the mean flow $\bar{\mathbf{U}}$.

We carry out a stability analysis in the local setting, neglecting x-variation of the mean flow. Hence, the ansatz for the perturbation has the form

$$\{u', v', w', p'\} = \{\hat{u}, \hat{v}, \hat{w}, \hat{p}\}(y, z)\mathrm{e}^{\mathrm{i}(\alpha x - \omega t)}. \tag{4.4}$$

Substituting the ansatz (4.4) into the linearised Navier–Stokes equation (4.3) with assumption of slow variation in the streamwise direction, the following stability problem

is established:

$$
\begin{aligned}
i\alpha\hat{u} + \frac{\partial\hat{v}}{\partial y} + \frac{\partial\hat{w}}{\partial z} &= 0,\\
-\bar{U}\alpha\hat{u} + \xi\hat{u} + i\hat{v}\frac{\partial\bar{U}}{\partial y} + i\hat{w}\frac{\partial\bar{U}}{\partial z} - \alpha\hat{p} + \alpha^2\frac{i}{Re}\hat{u} &= -\omega\hat{u},\\
-\bar{U}\alpha\hat{v} + \xi\hat{v} + i\hat{v}\frac{\partial\bar{V}}{\partial y} + i\hat{w}\frac{\partial\bar{V}}{\partial z} - \frac{\hat{p}}{y} + \alpha^2\frac{i}{Re}\hat{v} &= -\omega\hat{v},\\
-\bar{U}\alpha\hat{w} + \xi\hat{w} + i\hat{v}\frac{\partial\bar{W}}{\partial y} + i\hat{w}\frac{\partial\bar{W}}{\partial z} - \frac{\hat{p}}{z} + \alpha^2\frac{i}{Re}\hat{w} &= -\omega\hat{w},\\
\xi = i\bar{V}\frac{\partial}{\partial y} + i\bar{W}\frac{\partial}{\partial z} - \frac{i}{Re}&\left(\frac{\partial^2}{\partial y^2} + \frac{\partial^2}{\partial z^2}\right).
\end{aligned}
\tag{4.5}
$$

Letting $\mathbf{q} = \{\hat{u},\, \hat{v},\, \hat{w},\, \hat{p}\}^T$, the equation system can be rearranged to

$$
\left(\alpha\mathcal{A}_1 + \alpha^2\mathcal{A}_2\right)\mathbf{q} = (\omega\mathcal{B} - \mathcal{A}_0)\,\mathbf{q}, \tag{4.6}
$$

where $\mathcal{A}_0$, $\mathcal{A}_1$, $\mathcal{A}_2$ and $\mathcal{B}$ are functions of the mean flow and flow parameters. Following the spatial stability ansatz, we take $\omega \in \mathcal{R}$ to be the temporal frequency input while $\alpha \in \mathcal{C}$ is the complex output eigenvalue. Notice that a nonlinear term α^2 appears in the formulation. Thus, a linear eigenvalue problem, considering an eigenfunction given by $[\mathbf{q},\, \alpha\mathbf{q}]$, is solved instead (Bridges & Morris 1984; Piot, Casalis & Rist 2008).

The effect of roughness-generated streaks is investigated through tracking the unstable modes from the mean state without roughness elements to that with roughness elements (Lajús *et al.* 2019) by a continuous variation of the mean flow ($\bar{\mathbf{U}}$) as

$$
\bar{\mathbf{U}} = (1-\sigma)\bar{\mathbf{U}}_{clean} + \sigma\bar{\mathbf{U}}_{rough}, \tag{4.7}
$$

where $0 \leqslant \sigma \leqslant 1$. The tracking mode technique aids in identifying the growth rate changes between two distinct states. Ideally, a continuous change of the parameter σ allows us to trace the progression of an unstable mode through these states. For the sake of reducing computational effort, we utilise five discrete values of σ, which are sufficient to demonstrate the evolution of the eigenvalues. The spectrum is illustrated in figure 14. As can be seen there, there are three unstable modes in the clean case. The most unstable mode stands for two-dimensional K–H instability, with the mode shape depicted in the right-hand subplot of figure 15. The other two modes have identical low growth rate and streamwise wavenumber, corresponding to degenerate oblique K–H modes with positive and negative spanwise wavenumbers, as in Lajús *et al.* (2019). With an increase in the value of the parameter σ, the growth rate of the most unstable mode is decreasing from $\alpha_i = 0.1699$ to $\alpha_i = 0.1231$. However, the other two unstable modes in the clean state diverge and become more unstable with increasing σ. Two other modes appear from the stable regime, becoming unstable as σ approaches 1.

The shapes of the most unstable mode for various values of σ are presented in figure 15. Note that the eigenvectors are normalised with respect to the maximum value of streamwise velocity component $\tilde{u}$ at each σ value. From the clean state ($\sigma = 0$) to the rough state ($\sigma = 1$), a progressive spanwise modulation appears at the middle of domain. The K–H mode is heavily modulated in this region. The black dashed line denotes the critical layer, where $U = \omega/\alpha$, which is the location where the modulated modes peak. The appearance of streaks increases the amplitude of the spanwise velocity component $\tilde{w}$ while it decreases the strength of the wall-normal velocity component $\tilde{v}$.

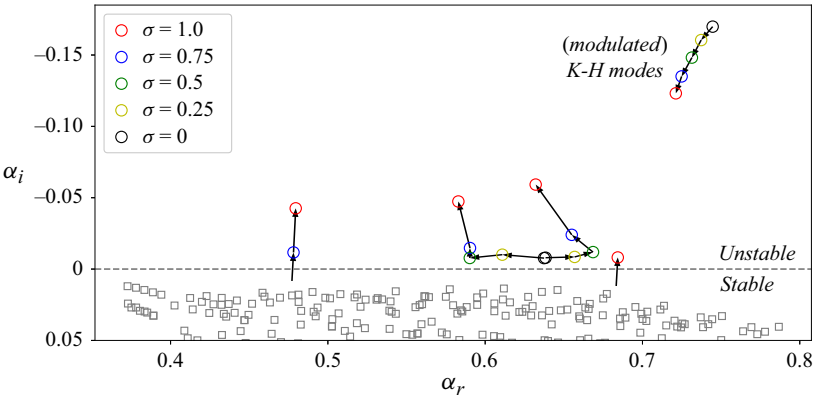

Figure 14. The spectrum traced with a gradual increase of the mean state modulation parameter σ. Open circles stand for the unstable modes and open squares represent stable modes.

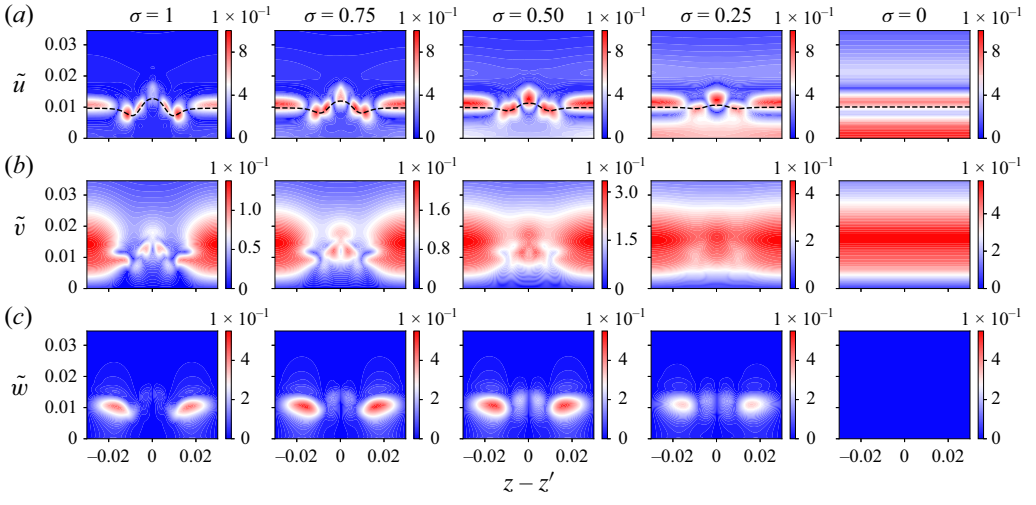

Figure 15. The leading eigenmodes (K–H modes) traced with gradual increase of mean state modulation parameter σ. Here σ changes from 1 to 0 from left to right. (*a*), (*b*) and (*c*) rows present the velocity components $\tilde{u}$, $\tilde{v}$ and $\tilde{w}$, respectively. Black dashed line indicates the critical layer.

Comparing the eigenmode for $\sigma = 1$ with the leading SPOD mode at the same station, the modes show many similarities, indicating that the SPOD mode is indeed representative of a spanwise-modulated K–H roller. We also extend the stability analysis to the upstream station $x/c = 0.70$ for both Reynolds numbers, as presented in Appendix D. The results suggest the same trend that the growth rate of the modulated K–H mode decreases with the increasing modulation of the mean flow made by streaks.

4.3. *Spectral proper orthogonal decomposition versus local stability analysis*

From the spatial stability analysis, it can be concluded that streaks can be used to decrease the growth of K–H instabilities. However, we are using the mean flow rather than the base state of the flow due to the difficulty of getting a laminar solution in the present setting. In order to verify this result, one can calculate the growth of hydrodynamic waves from the leading SPOD mode. Nonetheless, due to the existence of strong acoustic waves in

the field, SPOD modes contain energy of the hydrodynamic and acoustic perturbations. In order to extract hydrodynamic energy from the total energy, we utilise the bi-orthogonality of state and adjoint eigenfunctions (see e.g. Tumin 2011; Shahriari, Hanifi & Henningson 2016). In order to use our existing tool, we consider the problem in the framework of temporal stability analysis. Consider the direct and adjoint problem in a compact form as

$$\mathbf{Nq} = \omega \mathbf{Mq}, \tag{4.8}$$

$$\mathbf{N}^{+}\mathbf{q}^{+} = \omega^{+}\mathbf{M}^{+}\mathbf{q}^{+}, \tag{4.9}$$

where superscript $+$ indicates the adjoint and $\omega^{+} = \mathrm{conjg}(\omega)$. Let us define the weighted inner product with operator $\mathbf{M}$ as the weight operator as

$$\langle \mathbf{a}, \mathbf{b} \rangle_{\mathbf{M}} = \langle \mathbf{Ma}, \mathbf{b} \rangle = \int_{z_{min}}^{z_{max}} \int_{0}^{\infty} \mathbf{b}^{H} \mathbf{Ma} \, \mathrm{d}y \, \mathrm{d}z, \tag{4.10}$$

where H denotes complex conjugate transpose. Then the bi-orthogonality yields

$$\langle \mathbf{q}_i, \mathbf{q}_j^{+} \rangle_{\mathbf{M}} = \mathcal{E} \delta_{ij}, \tag{4.11}$$

where δ_{ij} is the Kronecker delta function and $\mathcal{E}$ is an arbitrary constant. Therefore, by projecting the LES solution onto the adjoint of hydrodynamic modes, one extracts their amplitude (Rodríguez *et al.* 2015). The amplitude of the hydrodynamic wave, C_h, at each x location can be evaluated through

$$C_h = \frac{\langle \hat{\boldsymbol{\Phi}}, \mathbf{q}_h^{+} \rangle_{\mathbf{M}}}{\langle \mathbf{q}_h, \mathbf{q}_h^{+} \rangle_{\mathbf{M}}}. \tag{4.12}$$

Here, $\mathbf{q}_h$ is the eigenvector corresponding to the hydrodynamic mode and $\hat{\boldsymbol{\Phi}} = \langle \hat{\rho}_s, \hat{u}_s, \hat{v}_s, \hat{w}_s, \hat{T}_s \rangle$ is the vector containing the SPOD mode. The denominator in (4.12) can be considered as a normalisation constant for the adjoint eigenfunction at each station. It is also important to note that the computed hydrodynamic mode amplitudes depend on the normalisation of the direct hydrodynamic eigenmode. Here, we have normalised hydrodynamic eigenmode, $\mathbf{q}_h$, with maximum streamwise velocity.

The eigenvalues of the direct and adjoint analysis are illustrated in figure 16 at $x/c = 0.75$. The complex-conjugated adjoint eigenvalues overlap with the direct eigenvalues which indicates the convergence of mesh and resolution. The frequencies of the unstable modes correspond to the tonal frequency and a modulated K–H mode, $St = 5.5$, and possibly to a secondary instability of streaks, $St = 3.9$. The mode corresponding to the modulated K–H mode is shown in figure 17. The direct mode is closely aligned with the spatial and SPOD analyses. Furthermore, the adjoint mode reveals the sensitivity of flow, and the least unstable mode indicates sensitivity of the spanwise-modulated K–H instability.

Five close stations $x/c = 0.75, 0.75 \pm 4 \times 10^{-4}, 0.75 \pm 8 \times 10^{-4}$ are used to calculate the spatial growth of K–H modes around the station $x/c = 0.75$. For this purpose, first, the amplitude of the dominant K–H mode is extracted at these stations using the projection given in (4.12). Then the maximum absolute value of the spanwise-averaged velocity field (to extract the two-dimensional K–H mode) is used to calculate the growth rate as

$$\text{Growth rate} = \frac{1}{|u|_{max}} \frac{\mathrm{d}|u|_{max}}{\mathrm{d}x}. \tag{4.13}$$

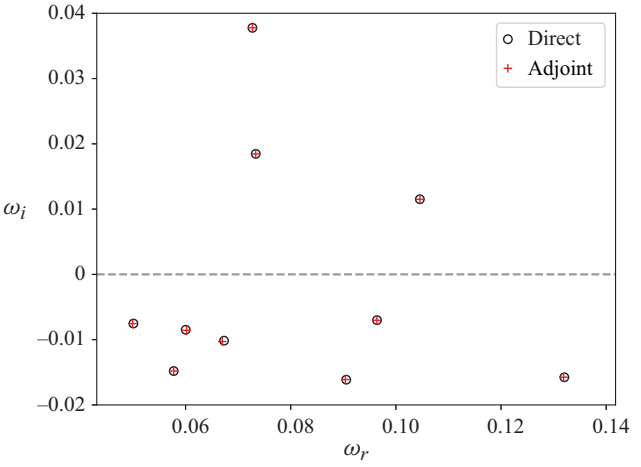

Figure 16. Eigenvalues of direct and adjoint modes calculated at the station $x/c = 0.75$. Note that adjoint eigenvalues are complex-conjugated.

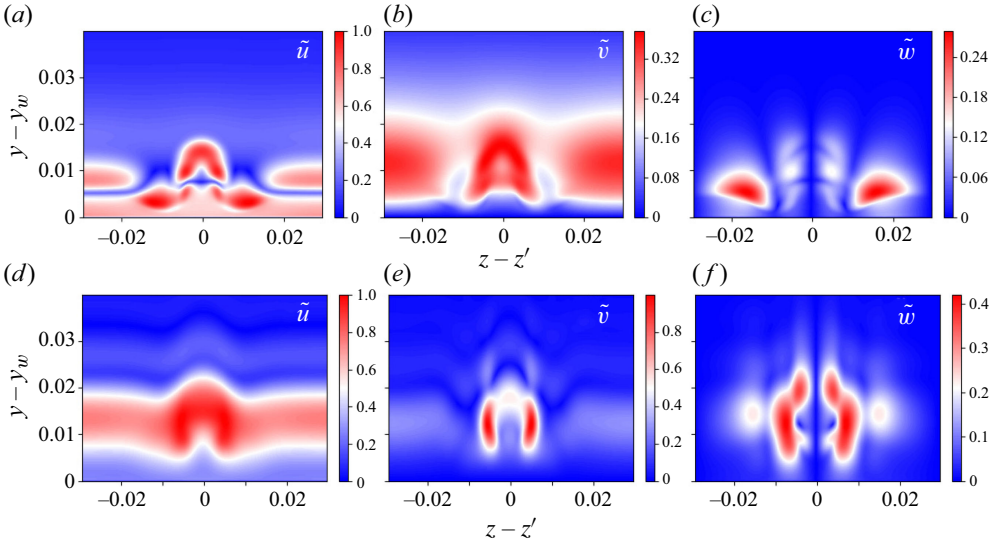

Figure 17. The absolute value of the modulated K–H mode calculated at the station $x/c = 0.75$. From (a) to (c) and (d) to (f): velocity components $\tilde{u}$, $\tilde{v}$ and $\tilde{w}$. (a–c): direct mode; (d–f): adjoint mode.

The results are listed in table 1. As can be seen there, the projected growth rates of the K–H mode are very close to the prediction given by the spatial stability analysis. This confirms the proposed mechanism for reduction of tonal noise: the introduction of roughness elements induces steady streaks, which render the laminar separation bubble three-dimensional, creating a spanwise modulation of the K–H instability of the shear layer, with a significant reduction of the growth rate. This weakens one of the components of the feedback loop leading to tonal airfoil noise, reducing tones emitted to the far field.

$Re = 80$k	(Clean) Stability	(Clean) SPOD	(Rough) Stability	(Rough) SPOD
Growth rate	0.1699	0.1613	0.1231	0.1201

Table 1. Growth rate at station $x/c = 0.75$ from spatial stability analysis and projected SPOD modes via (4.12) for both clean ($\sigma = 0$) and rough ($\sigma = 1$) states.

5. Conclusion

In this article, we report the numerical results of investigations of tonal trailing-edge noise of a NACA 0012 and its control. We have used surface roughness elements to attenuate amplitudes of the far-field acoustics. We have performed a series of wall-resolved LES with the spectral-element solver PyFR with and without surface roughness elements at two Reynolds numbers ($Re = 80\,000$ and $1\,00\,000$). The acoustic spectrum illustrates trends similar to those observed in the experiments in our companion work (Alva *et al.* 2023). For the clean geometry, the acoustic spectrum is dominated by the main tone ($St = 5.5$ for $Re = 80$k and $St = 5.2$ for $Re = 100$k). With the presence of roughness elements, in the lower-Re case, the main tone splits into multiple tones spread over a wider frequency regime. These tones have lower amplitude than the main tone in the clean case. At higher Re, the tonal noise is eliminated from the spectrum and a broadband spectrum is identified.

Plots of Q-criterion iso-surface contours indicate that two-dimensional spanwise-coherent structures (K–H rollers) are the dominant flow structures over the clean airfoil surface and the main source of radiated acoustics, as shown in the literature (Pröbsting *et al.* 2015; Ricciardi *et al.* 2022). The introduction of roughness elements leads to the formation of streamwise-elongated structures, which can be identified further downstream as streaks. These streaks modulate the K–H rolls, reducing their spanwise coherence. At higher Re, an early transition of these structures into three-dimensional forms occurs. Tonal noise is two-dimensional and according to the scattering condition (Nogueira *et al.* 2017), lower spanwise coherence is expected to decrease the amplitude of the tonal noise. Furthermore, the skin friction coefficient C_f illustrates that a long separation bubble exists from around 65 % of the chord until the trailing edge. The presence of the roughness element modulates and slices this separation bubble into subdomains and pushes the re-attachment point further upstream. The amplified and modulated K–H roller breaks down earlier on the airfoil surface, which generates structures with low spanwise coherence; this weakens one of the components of the feedback loop leading to tonal noise. For higher Re, the streaks are even stronger which results in even lower spanwise coherence close to the trailing edge.

The SPOD method has been employed to analyse dominant flow structures at a series of streamwise stations. At lower Re, the leading SPOD mode is consistent with a K–H instability modulated in the spanwise direction by the presence of streaks. Two-dimensional spatial stability analysis is performed at the streamwise station $x/c = 0.75$ where the spanwise-modulated K–H mode is well developed according to the SPOD analysis. The spatial stability analysis is performed on the weighted average of mean flow states between the clean geometry and the rough geometry controlled by the shape factor σ. By assigning various σ values, we can track unstable modes between two states. Results illustrate that the existence of streaks attenuates the growth of K–H instability from 0.1699 to 0.1231. This result is then confirmed via calculating the growth rate from SPOD modes. The SPOD modes contain a large portion of energy associated with the acoustic field. Hence, to separate the hydrodynamic energy from the acoustic energy, we employed a bi-orthogonality relation to extract the amplitude of the K–H mode from the

leading SPOD mode. The result showed that the growth of K–H instability from the clean geometry to the rough geometry decreases from 0.1613 to 0.1201, which is very close to the prediction of the stability analysis. This reduction of growth rate provides a first evidence of the mechanism reducing tonal noise radiation, as at least one of the components of the feedback loop of the tonal airfoil noise is weakened. A more complete assessment would involve global analysis, which is a promising direction for future work.

Overall, the analysis of the simulations presented in this work contributes to a better understanding of the mechanisms behind tone attenuation and suppression, as discussed in the experiments of our companion paper (Alva *et al.* 2023). The key aspects are related to the formation of streaks that render the laminar separation bubble three-dimensional, resulting in a spanwise modulation of K–H modes and a reduction of their growth rates. These effects are expected to weaken the feedback loop leading to tonal noise radiation. Future research can build on these theoretical insights to develop more refined designs of roughness elements aiming at the attenuation of the undesirable tonal noise from airfoils.

Supplementary movies. Supplementary movies are available at https://doi.org/10.1017/jfm.2025.10321.

Acknowledgements. The computations were performed on resources of the National Academic Infrastructure for Super-computing in Sweden (NAISS), at the LUMI super computer cluster in Finland and Dardel super computer at PDC KTH, Sweden.

Funding. Z.Y. would like to acknowledge the Swedish Research Council for supporting the current work under grant 2020-04084. E.A. would like to acknowledge CAPES, under the Brazilian Ministry of Education (MEC) for supporting experimental campaigns and FAPESP project for providing funding for equipment.

Declaration of interests. The authors report no conflict of interest.

Appendix A. Intervals of tonal frequencies

Compared with the experiments of Alva *et al.* (2023), the simulations use higher Mach numbers in order to speed up the statistical convergence. Such a Mach number difference leads to different tonal frequencies in simulation and experiment. A possibility to verify consistent behaviour in the simulation and experiment is to compare the frequency interval between tones, as suggested by Pröbsting (2022). Arbey & Bataille (1983) modified the feedback loop condition for the permissible discrete tonal frequencies (f_n) proposed by Tam (1974):

$$f_n = \left(n + \frac{1}{2}\right) \frac{u_c}{L} \frac{1}{\left(1 + \frac{u_c}{a_\infty - U_\infty}\right)}, \quad n = 0, 1, 2, \ldots, \tag{A1}$$

where u_c is the convective speed of K–H instability and L is the feedback loop length, namely the distance between the trailing edge and the receptivity point of the instability waves. Parameter L contains geometrical information and, perhaps more importantly in this case, the influence from the FST intensity. The frequency interval $\Delta f = f_n - f_{n-1}$ can be further derived as

$$\Delta f = \frac{a_\infty}{L} \frac{\tilde{u}_c M(1 - M)}{1 - (1 - \tilde{u}_c)M}, \tag{A2}$$

where $\tilde{u}_c = u_c / U_\infty$. The frequency difference Δf thus depends on the Mach number and FST difference, and therefore changes in these parameters may lead to differences between simulations and experiments.

According to the linear stability analysis in § 4.2, two convective speeds of the K–H instability, $\tilde{u}_c = 0.45$ and 0.42, are obtained for $Re = 100$k and 80k, respectively. As these

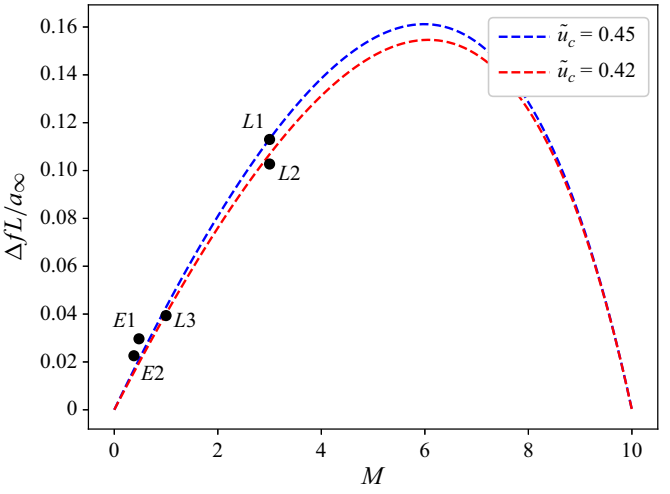

Figure 18. The non-dimensional tonal frequency interval. Here $L1$: $Re = 100$k clean, $M = 0.3$; $L2$: $Re = 80$k clean, $M = 0.3$; $L3$: $Re = 80$k clean, $M = 0.1$; $E1$: $Re = 100$k clean, $M = 0.0477$; $E2$: $Re = 80$k clean, $M = 0.0379$; L and E represent numerical and experimental data, respectively. Dashed lines are obtained from the second fraction on the right-hand side of (A2) using different convection speed.

values are not readily available in the wind tunnel measurements, we consider the same convection speed for the experimental results. The feedback loop length L is determined by the maximum boundary-layer edge velocity point on the airfoil (Arbey & Bataille 1983), namely $L_{LES} = 0.86c$ and $L_{Exp} = 0.78c$. The local stability analysis, where the velocity profiles from the streamwise stations are used to find the location of the unstable K–H instability, further confirms this feedback loop length in the numerical dataset. With these parameters, the relation between the non-dimensional frequency interval $\Delta f L/a_\infty$ and Mach number is presented in figure 18.

The tonal frequency interval shows a good agreement with Arbey and Bataille's model, despite the Mach number difference and the FST intensity between the simulations and the experiments. The present comparison thus shows that both experiment and simulation follow the behaviour in Arbey and Bataille's model; thus, the changes in tonal frequency difference between experiment and simulation are likely due to changes in Mach number and receptivity positions.

Appendix B. Mach number influence of the tonal noise generation

As mentioned in § 3, the simulations are performed under the same Reynolds number as for the experiments in Alva *et al.* (2023), but with different Mach number to avoid excessive computational cost. In this appendix, we study the effect of Mach number on the tonal noise generation and the feedback loop, attempting to verify if some of the discrepancies between simulation and experiment may be attributed to the Mach number difference. A new simulation with $Re = 80$k and $M = 0.1$ is performed to compare against the baseline $Re = 80$k clean case. Since a much lower Mach number is applied, a long time series is sampled with the same sampling frequency as mentioned in § 2, to make sure that more than 80 flow overs are obtained for data analysis. Notice that this lower Mach number is still significantly higher than those in the experiment (0.038 and 0.048 for $Re = 80$k and 100k, respectively); thus, the main purpose of this appendix is to verify quantitative changes to flow statistics that may be attributed to Mach number effects.

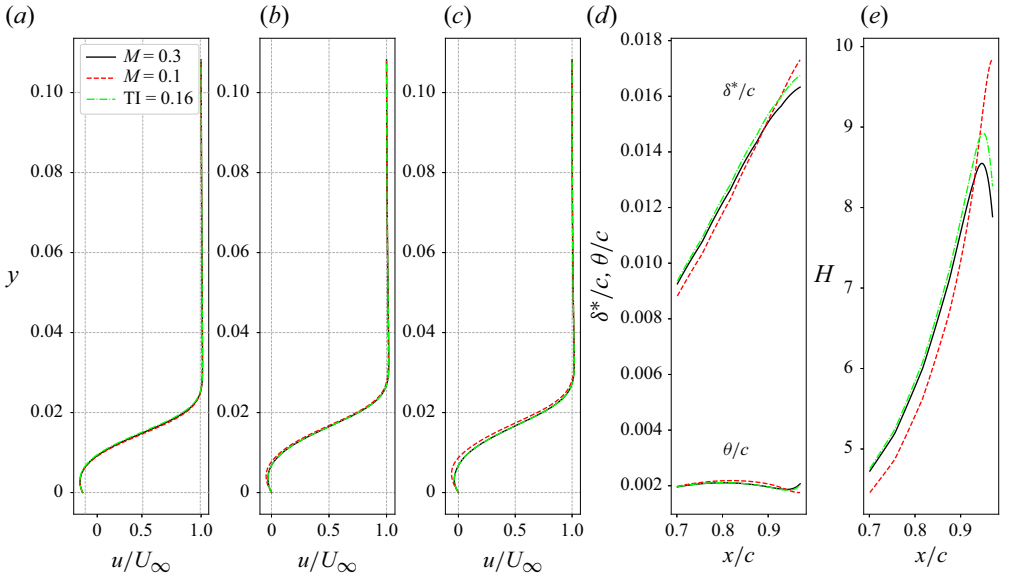

Figure 19. Boundary-layer characteristics for baseline case ($M = 0.3$, TI $= 0.0$, ——), low-Mach-number case ($M = 0.1$, TI $= 0.0$, - - -) and the FST case ($M = 0.3$, TI $= 0.16$, -·-·-). From (*a*) to (*e*): boundary-layer profiles at $x/c = 0.88$, 0.94, 0.97; the displacement thickness (δ^*/c) and momentum thickness θ/c; and the shape factor H.

Figure 19 shows the boundary-layer characteristics for both Mach numbers. The boundary-layer profiles indicate that a stronger reverse flow occurs in the $M = 0.1$ case. This phenomenon is more pronounced at the location $x/c = 0.97$. The displacement thickness δ^*/c is slightly thicker for the case $M = 0.1$ up to the location $x/c = 0.9$, while the momentum thickness θ/c shows a local minimum close to the trailing edge for the same case. The shape factor for the case $M = 0.1$ peaks upstream of the trailing edge, while the case $M = 0.3$ shows a monotonically increasing shape factor. The decreasing shape factor in the low-Mach-number case implies that the flow gradually undergoes a transition involving vortex shedding and breakup. These observations are in good agreement with findings in Pröbsting (2022). Figure 20 shows the pressure coefficient c_p, the skin friction coefficient c_f and the mean wake velocity profile. Coefficient c_p shows good agreement for both Mach numbers. Coefficient c_f indicates that the separation location is further upstream for the case $M = 0.1$ but both cases have the same reattachment locations. Ricciardi *et al.* (2020) also observed an increase of the laminar separation bubble with increasing Mach number from $M = 0.1$ to $M = 0.3$ using the same Reynolds number and angle of attack as discussed here. The mean wake profile shows a certain degree of agreement, but it cannot be excluded that the shapes are not identical. As discussed in Pröbsting (2022), the observed differences can be attributed to the influence of the Mach number on the mean flow which occurs as a result of a modified vortex-shedding process.

Furthermore, the acoustic spectra for both cases are presented in figure 21. The main tone frequencies are $St = 5.5$ for the case $M = 0.1$ and $St = 5.2$ for the case $M = 0.3$. The main tone frequency is shifted towards the lower-frequency regime with increasing Mach number. Moreover, the PSD amplitude increases on moving from $M = 0.1$ to $M = 0.3$. Ricciardi *et al.* (2020) also observed the PSD level of the dominant peak of the velocity fluctuations to generally increase with an increase in the Mach number.

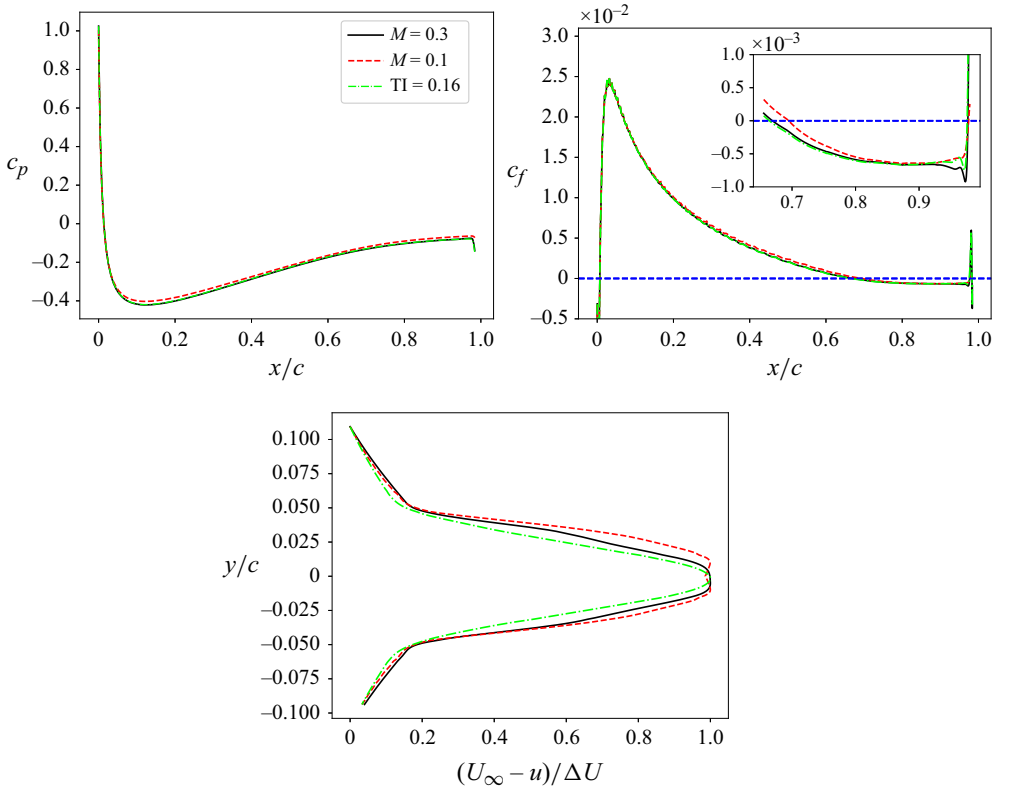

Figure 20. Surface pressure coefficient c_p, skin friction coefficient c_f and mean wake velocity profile obtained at $x/c = 1.1$ for baseline case ($M = 0.3$, TI $= 0.0$, ——), low-Mach-number case ($M = 0.1$, TI $= 0.0$, - - -) and the FST case ($M = 0.3$, TI $= 0.16$, -·-·-).

Overall, for the simulations with the two considered Mach numbers, the boundary-layer characteristics and acoustic spectrum features are similar, but present some quantitative differences: laminar separation bubbles exist in the region close to the trailing edge, but the size of separation bubbles varies with Mach number; in the acoustic spectrum, the typical ladder-type structure with dominant and secondary tones can be identified for both Mach numbers, but the main tone frequencies are shifted and amplitudes are different. Hence, the observed quantitative differences may explain the discrepancies between the Mach 0.3 simulation and the experiments in Alva *et al.* (2023). However, as there are similarities of the main characteristics of flow and acoustic radiation for Mach 0.1 and 0.3, we expect the dominant physical mechanisms studied in this work to be similar to those of the experiments of Alva *et al.* (2023).

Appendix C. Free-stream turbulence influence of the tonal noise generation

Another major difference between the simulation and experiments is the FST level. In this appendix, the influence of the FST is discussed. A simulation with FST is performed with $Re = 80$k, Mach $= 0.3$ and baseline geometry. The turbulence intensity is chosen to be TI $= 0.16\,\%$ which is aligned with the experimental measurement. The boundary-layer characteristics, c_p, c_f and the mean wake velocity profile are presented in figures 19 and 20. From the boundary-layer measurement, the FST shows very limited influence on the boundary layer as TI is very low. A slight increment of the displacement and

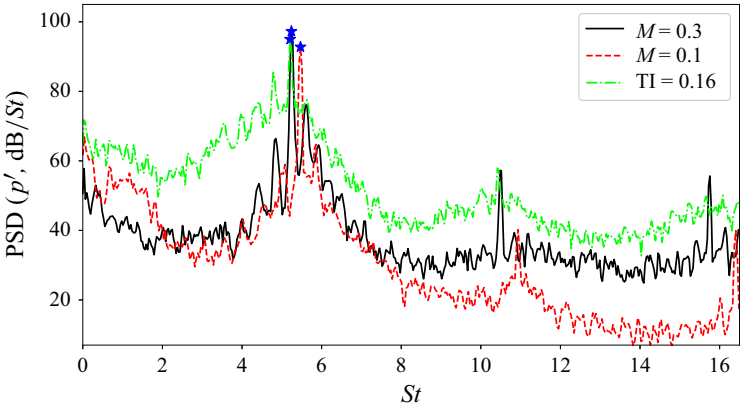

Figure 21. Acoustic spectra obtained at $x/c = 1$ and $y/c = 1$ for baseline case ($M = 0.3$, TI $= 0.0$, ——), low-Mach-number case ($M = 0.1$, TI $= 0.0$, - - -) and the FST case ($M = 0.3$, TI $= 0.16$, -·-·-). The stars represent the dominant tones at frequencies $St = 5.2$ (baseline/FST case) and $St = 5.5$ (low-Mach-number case).

momentum thickness can be seen for the case with FST. The mean pressure distribution and the location and length of the separation bubble are very similar regardless of the FST. The wake profile shows the larger difference. Similar to the Mach number influence on the mean wake profile, this can be attributed to the modification of the vortex shedding process by FST on the mean flow.

The acoustic spectrum is presented in figure 21. The case with FST has a slightly lower tonal frequency compared with the baseline case. However, there is a noticeable increment of the energy of all non-tonal frequencies presented in the FST case. Note that the contribution could come from the vortical structure on the airfoil and also from the FST generator of the solver since it acts as a source term. The acoustic energy at the tonal frequency is lower than in the baseline case because the FST enters the boundary layer and weakens the spanwise coherence of the K–H rolls.

Overall, the FST with small TI has a limited influence on the physical mechanisms studied in this work. More influence could come from the defects of the airfoil model used in the experimental work of Alva *et al.* (2023), i.e. gaps of the interchangeable strips with/without roughness elements. Tapes are used to smooth the gaps but the separation bubbles are sensitive to the changes of the flow.

Appendix D. Local spatial stability analysis at $x/c = 0.7$

In this appendix we perform the local spatial stability analysis (4.6) of the upstream station $x/c = 0.70$ for both Reynolds numbers as a comparison and complement to § 4.2. As in § 4.2, the mean flow states between the clean ($\sigma = 1$) and the rough ($\sigma = 0$) are used for tracking the (modulated) K–H modes.

Figure 22(a) shows the spectrum and the leading eigenmodes (modulated K–H modes) from the stability analysis for the case $Re = 80$k. Compared with the results from figure 14, the most unstable eigenvalue for the clean case ($\sigma = 1$) shows a higher growth rate at the upstream station $\alpha_i = 0.2570$ compared with $\alpha_i = 0.1699$ at the downstream station. For the rough case ($\sigma = 1$), both cases show a similar growth rate, $\alpha_i = 0.1241$ for $x/c = 0.70$ and $\alpha_i = 0.1231$ for $x/c = 0.75$. In other words, the streaks lead to a stronger reduction of growth rates at the upstream station for the case $Re = 80$k. The modulated K–H modes are shown in the right-hand columns of figure 22(a). Similar to the trend of the results from $x/c = 0.75$, a progressive spanwise modulation appears from $\sigma = 0$ to 1.

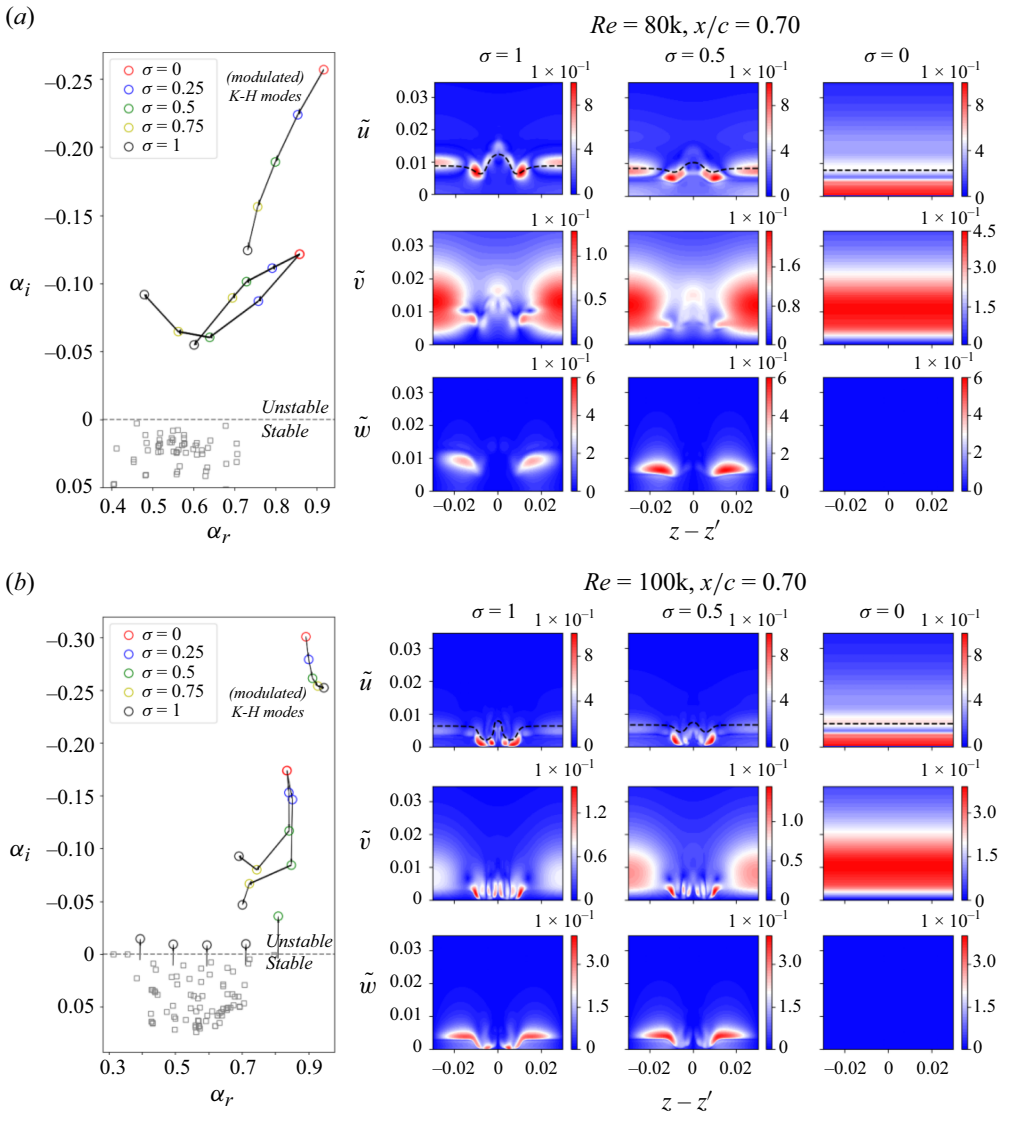

Figure 22. (*a*): the spectrum traced with the increase of mean state modulation parameter σ. Open circles stand for the unstable modes and open squares are stable modes. (*b*): the leading eigenmodes (K–H modes). Top, middle and bottom rows represent the velocity components $\tilde{u}$, $\tilde{v}$ and $\tilde{w}$, respectively. Black dashed line indicates the critical layer. (*a*) Case $Re = 80$k and (*b*) case $Re = 100$k.

The spanwise velocity $\tilde{w}$ increases between $\sigma = 1$ and 0.5, but decreases when $\sigma = 1$. The normal velocity $\tilde{v}$ decreases when the mean flow is modulated by the roughness elements.

Figure 22(*b*) presents the spectrum and the leading eigenmodes for $Re = 100$k. The spectrum shows trends similar to those in the case of $Re = 80$k: the growth rate of the K–H instability is reduced when modulated by streaks. However, as the modulation parameter σ is increased, the streamwise wavenumber of the least unstable mode increases. Two eigenmodes corresponding to the degenerate K–H modes appear at $\sigma = 0$ and both modes become more stable at $\sigma = 1$. The eigenmodes at both stations show a strong K–H mode at $\sigma = 1$. As σ increases to 1, a strong modulation is observed near the wall in the centre of the domain. Compared with $Re = 80$k, stronger streaks show a more significant

modulation of the K–H modes. This can also be observed in the mean flow visualisation in figure 10. However, due to the higher Reynolds number, the breakdown of the streaks induces a turbulent state in the rough case of $Re = 100$k, as can be seen in figure 7 and the supplementary movies. This explains the broadband-type acoustic spectrum for this case.

Overall, the stability analysis of the three cases here shows that the presence of the streaks modulates the K–H mode. The growth rate of the K–H mode decreases as more modulation is applied to the mean flow.

References

Alva, R.E., Yuan, Z., Araujo, T., Amaral, F.R., Hanifi, A. & Cavalieri, A.V. 2023 *Reduction of tonal noise of a NACA, 0012 airfoil by roughness elements*. American Institute of Aeronautics and Astronautics.

Arbey, H. & Bataille, J. 1983 Noise generated by airfoil profiles placed in a uniform laminar flow. *J. Fluid Mech.* **134** (1), 33–47.

Arcondoulis, E.J.G., Doolan, C.J., Zander, A.C. & Brooks, L.A. 2010 A review of trailing edge noise generated by airfoils at low to moderate Reynolds number. *Acoust. Austral.* **38** (3), 129–133.

Bagheri S. & Hanifi A. 2007 The stabilizing effect of streaks on Tollmien–Schlichting and oblique waves: a parametric study. *Phys. Fluids* **19** (7), 078103.

Berkooz, G., Holmes, P. & Lumley, J.L. 1993 The proper orthogonal decomposition in the analysis of turbulent flows. *Annu. Rev. Fluid Mech.* **25** (1), 539–575.

Bodony, D.J. 2006 Analysis of sponge zones for computational fluid mechanics. *J. Comput. Phys.* **212** (2), 681–702.

Brandt, L. 2014 The lift-up effect: the linear mechanism behind transition and turbulence in shear flows. *Eur. J. Mech. - B/Fluids* **47** (47), 80–96.

Bridges, T.J. & Morris, P.J. 1984 Differential eigenvalue problems in which the parameter appears nonlinearly. *J. Comput. Phys.* **55** (3), 437–460.

Brooks, T.F. & Marcolini, M.A. 1985 Scaling of airfoil self-noise using measured flow parameters. *AIAA J.* **23** (2), 207–213.

Brooks, T.F., Pope, D.S. & Marcolini, M.A. 1989 Airfoil self-noise and prediction. *NASA Tech. Rep.*, 1–146.

Chen, W., Qiao, W., Wang, X., Wang, L. & Tong, F. 2016 An experimental and numerical investigation of airfoil instability noise with leading edge serrations. In *22nd AIAA/CEAS Aeroacoustics Conference*, pp. 2956. American Institute of Aeronautics and Astronautics.

Chu, B.-T. 1965 On the energy transfer to small disturbances in fluid flow (part i). *Acta Mechanica* **1** (3), 215–234.

Cossu C. & Brandt L. 2002 Stabilization of Tollmien–Schlichting waves by finite amplitude optimal streaks in the Blasius boundary layer. *Phys. Fluids* **14** (8), L57–L60.

Cossu, C. & Brandt, L. 2004 On Tollmien–Schlichting-like waves in streaky boundary layers. *Eur. J. Mech. - B/Fluids* **23** (6), 815–833.

Curle, N. 1955 The influence of solid boundaries upon aerodynamic sound. *Proc. R. Soc. Lond. A. Math. Phys. Sci.* **231**(1187), 505–514.

Demange, S., Yuan, Z., Jekosch, S., Hanifi, A., Cavalieri, A.V.G., Sarradj, E., Kaiser, T.L. & Oberleithner, K. 2024*a* Resolvent model for aeroacoustics of trailing edge noise. *Theor. Comput. Fluid Dyn.* **38** (2), 163–183.

Demange, S., Yuan, Z., Jekosch, S., Hanifi, A., Cavalieri, A.V.G., Sarradj, E., Kaiser, TL. & Oberleithner, K. 2024*b* Resolvent model for aeroacoustics of trailing edge noise. *Theor. Comput Fluid Dyn.* **38** (2), 163–183.

Desquesnes, G., Terracol, M. & Sagaut, P. 2007 Numerical investigation of the tone noise mechanism over laminar airfoils. *J. Fluid Mech.* **591**, 155–182.

Ellingsen, T. & Palm, E. 1975 Stability of linear flow. *Phys. Fluids* **18** (4), 487–488.

Ffowcs Williams, J.E. & Hall, L.H. 1970 Aerodynamic sound generation by turbulent flow in the vicinity of a scattering half plane. *J. Fluid Mech.* **40** (4), 657–670.

Fosas de Pando, M., Schmid, P J. & Sipp, D. 2014 A global analysis of tonal noise in flows around aerofoils. *J. Fluid Mech.* **754** (september), 5–38.

Fransson J.H.M., Brandt L., Talamelli A. & Cossu C. 2004 Experimental and theoretical investigation of the nonmodal growth of steady streaks in a flat plate boundary layer. *Phys. Fluids* **16** (10), 3627–3638.

FRANSSON J.H.M., BRANDT L., TALAMELLI A. & COSSU C. 2005 Experimental study of the stabilization of Tollmien–Schlichting waves by finite amplitude streaks. *Phys. Fluids* **17** (5), 1–15.

FREUND, J.B. 1997 Proposed inflow/outflow boundary condition for direct computation of aerodynamic sound. *AIAA J.* **35** (4), 740–742.

HANIFI A., SCHMID P.J. & HENNINGSON D.S. 1996 Transient growth in compressible boundary layer flow. *Phys. Fluids* **8** (3), 826–837.

HANSEN, K., KELSO, R. & DOOLAN, C. 2010 *Reduction of Flow Induced Tonal Noise Through Leading Edge Tubercle Modifications*, American Institute of Aeronautics and Astronautics.

HOWE, M.S. 1991 Aerodynamic noise of a serrated trailing edge. *J. Fluid. Struct.* **5** (1), 33–45.

HOWE, M.S. 2001 Edge-source acoustic green's function for an airfoil of arbitrary chord, with application to trailing-edge noise. *Q. J. Mech. Appl. Math.* **54** (1), 139–155.

JEONG, J. & HUSSAIN, F. 1995 On the identification of a vortex. *J. Fluid Mech.* **285**, 69–94.

JONES, L. & SANDBERG, R. 2010 Numerical investigation of airfoil self-noise reduction by addition of trailing-edge serrations. In *16th AIAA/CEAS Aeroacoustics Conference*, pp. 1–1, American Institute of Aeronautics and Astronautics.

KARP, M. & HACK, M.J.P. 2020 Optimal suppression of a separation bubble in a laminar boundary layer. *J. Fluid Mech.* **892**, A23.

LAJÚS, F.C., SINHA, A., CAVALIERI, A.V.G., DESCHAMPS, C.J. & COLONIUS, T. 2019 Spatial stability analysis of subsonic corrugated jets. *J. Fluid Mech.* **876**, 766–791.

LANDAHL, M.T. 1980 A note on an algebraic instability of inviscid parallel shear flows. *J. Fluid Mech.* **98** (2), 243–251.

LUMLEY, J. L. 1970 *Stochastic Tools in Turbulence*. Academic Press.

MACK, L.M. 1984 Boundary layer stability theory. In *AGARD Conference Proceedings*, vol. 1, pp. 1–1–1–22. NATO.

MANOHA, E., TROFF, B. & SAGAUT, P. 2000 Trailing-edge noise prediction using large-eddy simulation and acoustic analogy. *AIAA J.* **38** (4), 575–583.

MARANT, M. & COSSU, C. 2018 Influence of optimally amplified streamwise streaks on the Kelvin–Helmholtz instability. *J. Fluid Mech.* **838**, 478–500.

NOGUEIRA, P.A.S., CAVALIERI, A.V.G. & JORDAN, P. 2017 A model problem for sound radiation by an installed jet. *J. Sound Vib.* **391**, 95–115.

OERLEMANS, S., FISHER, M., MAEDER, T. & KÖGLER, K. 2009 Reduction of wind turbine noise using optimized airfoils and trailing-edge serrations. *AIAA J.* **47** (6), 1470–1481.

PARK, J.S., WITHERDEN, F.D. & VINCENT, P.E. 2017 High-order implicit large-eddy simulations of flow over a NACA0021 aerofoil. *AIAA J.* **55** (7), 2186–2197.

PATERSON, R.W., VOGT, P.G., FINK, M.R. & MUNCH, C.L. 1973 Vortex noise of isolated airfoils. *J. Aircraft* **10** (5), 296–302.

PICARD, C. & DELVILLE, J. 1999 Pressure velocity coupling in a subsonic round jet. In *Engineering Turbulence Modelling and Experiments* (ed. W RODI & D. LAURENCE), vol. 4, pp. 443–452, Elsevier Science Ltd.

PIOT, E., CASALIS, G. & RIST, U. 2008 Stability of the laminar boundary layer flow encountering a row of roughness elements: Biglobal stability approach and DNS. *Eur. J. Mech. - B/Fluids* **27** (6), 684–706.

PRÖBSTING, S. 2022 Effect of mach number on the aeroacoustic feedback loop generating airfoil tonal noise. *Phys. Fluids* **34** (9), 94–115.

PRÖBSTING, S., SCARANO, F. & MORRIS, S.C. 2015 Regimes of tonal noise on an airfoil at moderate Reynolds number. *J. Fluid Mech.* **780**, 407–438.

RICCIARDI, T.R., ARIAS-RAMIREZ, W. & WOLF, W.R. 2020 On secondary tones arising in trailing-edge noise at moderate Reynolds numbers. *Eur. J. Mech. - B/Fluids* **79**, 54–66.

RICCIARDI, T.R. & WOLF, W.R. 2022 Switch of tonal noise generation mechanisms in airfoil transitional flows. *Phys. Fluid Dyn.* **7** (8), 084701.

RICCIARDI, T.R., WOLF, W.R. & TAIRA, K. 2022 Transition, intermittency and phase interference effects in airfoil secondary tones and acoustic feedback loop. *J. Fluid Mech.* **937**, A23.

RODRÍGUEZ, D., CAVALIERI, A.V.G., COLONIUS, T. & JORDAN, P. 2015 A study of linear wavepacket models for subsonic turbulent jets using local eigenmode decomposition of piv data. *Eur. J. Mech. - B/Fluids* **49**, 308–321.

ROGER, M. & MOREAU, S. 2005 Back-scattering correction and further extensions of Amiet's trailing-edge noise model. Part 1: theory. *J. Sound Vib.* **286** (3), 477–506.

ROGER, M., SCHRAM, C. & DE SANTANA, L. 2013 Reduction of airfoil turbulence-impingement noise by means of leading-edge serrations and/or porous material. In *19th AIAA/CEAS Aeroacoustics Conference*, pp. 2108. American Institute of Aeronautics and Astronautics.

SANDBERG, R.D. 2013 Direct numerical simulations for flow and noise studies. *Procedia Engng* **61**, 356–362.
SANDBERG, R., JONES, L. & SANDHAM, N. 2008 Direct numerical simulations of noise generated by turbulent flow over airfoils. In *14th AIAA/CEAS Aeroacoustics Conference (29th AIAA Aeroacoustics Conference)*, pp. 1–1, American Institute of Aeronautics and Astronautics.
SANO, A., ABREU, L.I., CAVALIERI, A.V.G. & WOLF, W.R. 2019 Trailing-edge noise from the scattering of spanwise-coherent structures. *Phys. Rev. Fluids* **4** (9), 094602.
SCHMIDT, O.T. & COLONIUS, T. 2020 Guide to spectral proper orthogonal decomposition. *AIAA J.* **58** (3), 1023–1033.
SERSON, D., MENEGHINI, J.R. & SHERWIN, S.J. 2017 Direct numerical simulations of the flow around wings with spanwise waviness. *J. Fluid Mech.* **826**, 714–731.
SHAHRIARI, N., HANIFI, A. & HENNINGSON, D.S. 2016 *Application of Biorthogonal Eigenfunction System for Extraction of Tollmien-Schlichting Waves in Acoustic Receptivity Simulations*. KTH Royal Institute of Technology.
SINGER, B.A., BRENTNER, K.S., LOCKARD, D.P. & LILLEY, G.M. 2000 Simulation of acoustic scattering from a trailing edge. *J. Sound Vib.* **230** (3), 541–560.
TAM C.K.W. 1974 Discrete tones of isolated airfoils. *J. Acoust. Soc. Am.* **55** (6), 1173–1177.
TOWNE, A., SCHMIDT, O.T. & COLONIUS, T. 2018 Spectral proper orthogonal decomposition and its relationship to dynamic mode decomposition and resolvent analysis. *J. Fluid Mech.* **847**, 821–867.
TUMIN, A. 2011 The biorthogonal eigenfunction system of linear stability equations: A survey of applications to receptivity problems and to analysis of experimental and computational results. In *41st AIAA Fluid Dynamics Conference and Exhibit*, pp. 1–1, American Institute of Aeronautics and Astronautics (AIAA).
VATHYLAKIS, A., CHONG, T.P. & JOSEPH, P.F. 2015 Poro-serrated trailing-edge devices for airfoil self-noise reduction. *AIAA J.* **53** (11), 3379–3394.
WANG, M. & MOIN, P. 2000 Computation of trailing-edge flow and noise using large-eddy simulation. *AIAA J.* **38** (12), 2201–2209.
WELCH, P. 1967 The use of fast Fourier transform for the estimation of power spectra: A method based on time averaging over short, modified periodograms. *IEEE Trans. Audio Electroacoust.* **15** (2), 70–73.
WITHERDEN, F.D., FARRINGTON, A.M. & VINCENT, P.E. 2014 Pyfr: an open source framework for solving advection–diffusion type problems on streaming architectures using the flux reconstruction approach. *Comput. Phys. Commun.* **185** (11), 3028–3040.
YUAN, Z., DEMANGE, S., JEKOSCH, S., SARRADJ, E., OBERLEITHNER, K., CAVALIERI, A. & HANIFI, A. 2024 *Wavepackets Driving Trailing Edge Noise. Part I – Direct Simulation and Experiments*. American Institute of Aeronautics and Astronautics (AIAA), https://arc.aiaa.org/doi/pdf/10.2514/6.2024-3123.